ABSTRACT

Title of Dissertation:	BIO-INSPIRED PUMPING MECHANISMS IN AN INTERMEDIATE REYNOLDS NUMBER
	Farhad Saffaraval, Doctor of Philosophy 2018
Dissertation directed by:	Dr. Kenneth Kiger, Department of Mechanical Engineering

Pumps are important to applications across a wide range of scales. Most of traditional applications occur within a range where inertia is the dominating factor influencing the pump performance, and hence many practical designs are based on mechanisms that rely on this assumption. As one moves towards smaller devices, however, the increasing effect of viscosity renders these traditional mechanisms ineffective. The current work looks towards a bio-inspired system consisting of an array of oscillating plates to contend with this challenge. The plates are placed within a channel, and the pumping performance generated is examined for a small range of Reynolds numbers intermediate between inertial and viscous regimes ($0.1 < Re < 10$). The goal of this work is to observe the effect of how different plate kinematics can be utilized to break the symmetry the system to produce a net pumped flow. Rigid and flexible plates are studied, using both sinusoidal and triangle wave actuation kinematics. The tests are

first conducted with a single appendage, and then repeated with an array of 5 closely spaced plates to observe the effect of their interaction on the overall performance. The results of the single plate tests indicate that increased asymmetry introduced in the triangle wave actuation results in increased pumping performance as well as energy consumption. Tests were conducted at two Reynolds number conditions, Re = 0.6 and 6. The pumping performance was found to be an order of magnitude higher for the Re = 6 case. In the case of flexible plates, the results show that a mass specific pumping efficiency was higher for the flexible case with a higher frequency at the same Reynolds numbers. For the plate array, the results indicate five flexible plates with $\Delta\theta_i = -90$ will generate more than 4 times the flow rate in comparison to the single flexible plate. Asymmetric triangle actuation in conjunction with symplectic metachronal motion ($\Delta\theta_i = 30$) exhibits pumping performance more than 10 times of using a single rigid plate. Total work is noticeably higher for multiple plate system and will result in a reduced overall pumping efficiency in comparison to the single appendage.

BIO-INSPIRED PUMPING IN AN ARRAY OF OCSILLATING PLATES IN INTERMEDIATE REYNOLDS NUMBER REGIME

by

Farhad Saffaraval

Dissertation submitted to the Faculty of the Graduate School of the
University of Maryland, College Park, in partial fulfillment
of the requirements for the degree of
Doctor of Philosophy
2018

Advisory Committee:
Professor Kenneth Kiger, Chair
Professor James Duncan
Dr. Johan Larsson
Dr. Amir Riaz
Professor. James Baeder

Acknowledgements

I would like to thank Professor Kiger for his guidance and advises throughout this research. I also want to thank my family and friends who were beside me during hardships. I would like to express appreciation to the committee members who helped me improving this dissertation.

Table of Contents

List of Tables

List of Figures

List of Abbreviations

Re	Reynolds number
$Re_{eff\ (or\ rec)}$	Reynolds number during the effective (or recovery) stroke
ϕ	Root angle
$\Delta\Phi$	Amplitude of strokes
$\Delta\theta_i$	phase difference between adjacent plates
Φ_i	Plate's angle
ω	Angular velocity
T	The time period of the oscillation cycle
τ_e	Shear stress in the effective stroke
τ_r	Shear stress in the recovery stroke
f	frequency of strokes
f_r	Effective frequencies associated with the recovery stroke
f_e	Effective frequencies associated with the effective stroke
N	Number of PIV images
$N_{x\ (or\ y)}$	Number of values in the x (or y) direction
ν	Working fluid kinematic viscosity
U	characteristic velocity scale
U_{avg}	Average horizontal velocity

u_i	Instantaneous velocity within the discrete i_{th}PIV image
U_p (y)	gives a measure of the average velocity distribution with respect to channel height
$U_{normalized}$	Tip velocity in a beat cycle
ΔU_i	Calculated standard error
x	Streamwise direction
y	Wall-normal direction
Π	Pumping performance
H	Channel height
L	Channel length
l	Plates length
A	Amplitude
ε	Asymmetry parameter
ϵ_k	Asymmetry parameter
ϵ_0	Observed experimental asymmetry parameter
$\overline{E}$	The time averaged total work
E	Energy
e	strain
ρ	Density
g	gravity
δ	Kronecker Delta
$\Delta\delta x_i$	Uncertainty in the grid spacing

γ	Hinge angle
CW	Clockwise
CCW	Counter clockwise
MSVF	Mass-specific volume flux
FS	Flexible slow
FF	Flexible fast
RH	Rigid high
SF	Slow flexible
SAF	Sine/Antiplectic/flexible
TR	Triangle/rigid
TAR	Triangle/Antiplectic/rigid
TsR	Triangle/Symplectic/rigid

Chapter 1: Introduction and literature review

Animals have evolved through millions of years to generate flow for locomotion, reproduction, respiration, or feeding. Comparative studies have revealed a fundamental relationship between the dynamic scale of different species, as captured by the Reynolds number (Re), and patterns of appendicular movement (Strathmann 1993; Walker 2002).

The Reynolds number is the ratio of inertia effects to viscous effects in the fluid medium. $Re = \frac{UL}{\nu}$, where U is a characteristic velocity scale, L is characteristic length and ν is the fluid kinematic viscosity. In defining the Reynolds number for a given problem, one must carefully select the appropriate reference length and velocity scale. For simple problems such as pipe flow, U is typically defined as the mean flow in the pipe and L is defined to be the pipe diameter. However, for more complex problems, the definition of characteristic scales can be more difficult, and sometimes the problem cannot be simply defined with a single definition. For example, the pumping of fluid through a channel using oscillating plates permits two different possible definitions: one is a plate-based Reynolds number using the tip velocity and plate length to represent flow regime locally around plates, and second is a Reynolds number based on the mean flow velocity and channel width to characterize the entire channel flow regime. In the current project, we are looking at flow field around a single oscillating plate or array of multiple plates.

The Reynolds number for such a system can be defined as $Re=\frac{fl^2}{\nu}\Delta\Phi$ in which $f: frequency\ of\ strokes$, $\Delta\Phi: Amplitude\ of\ strokes$, $l: is\ plates\ length$, and $\nu: working\ fluid\ kinematic\ viscosity$ (Figure 1).

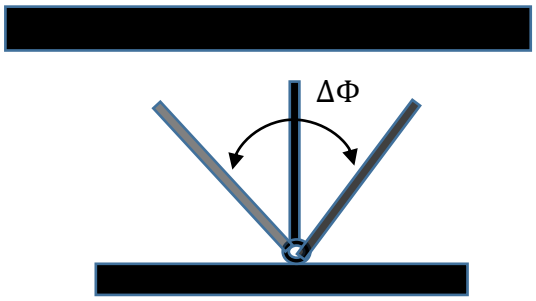

Figure 1.Schematic of oscillating plate in the channel

For the same working fluid, the form of the Reynolds number indicates that the inertia dominates at large animal sizes and high appendage velocities (Re >> 1), while viscous forces control the flow dynamics for small sizes or relatively low speed (Re << 1) (Taylor 1951; J. Lighthill 1976; Brennen and Winet 1977). In the two extremes of either very small (Re<<1) or very large Reynolds numbers (Re>>1000), mechanisms for flow generation by oscillating appendages are well described by theories based on Stokes flow or unsteady inviscid theory complemented by appropriate boundary layer effects (Spedding, Rosén, and Hedenström 2003; Motani 2002).

The extremes of these two regimes are also reflected in the broad spectrum of Reynolds number covered in the natural world, spanning a typical range of $10^{-5} < Re < 10^5$ **(**Table 1).

.

Table 1. Range of different Re-numbers seen in nature

Organism	Re-number	
A large whale swimming at 10 m/s	Very large Re-number	300000
A duck flying at 20 m/s	High Re-number	30000
Mayfly nymph	Intermediate Re-number	1-30
An invertebrate larva ,0.3 mm long, at 1mm/s	Low Re-number	0.3
A bacteria, swimming at 0.01 mm/s	Very small Re-number	0.00001

Fluid propulsion and pumping in sub-millimeter organisms is vital for their survival. For example, marine suspension feeders use cilia to propel food toward their bodies (Sleigh, Blake, and Liron 1988). Cilia are small hair-like structures with typical lengths between 4 to 12 μm and are probably the most universal biological mechanism to generate flow in low Reynolds numbers (Re<<1). Cilia beat in a periodic and non-reciprocal fashion and are often used in nature for fluid manipulations (Khaderi, den Toonder, and Onck 2012). Non-reciprocal motion is essential for pumping in–low Reynolds numbers, and therefore similar ciliary motion has been implemented in the lab-on-a-chip (LOC) devices. LOC is a device that integrates one or several laboratory functions in a millimeter-sized chip and is used to handle a small amount of fluid (on the order of pico-liters) in the low Reynolds number realm. LOC devices are miniature in size with applications in chemical analysis and biological assays and even medical diagnoses. In addition to their smaller size, there are variety of advantages for these devices. They offer faster speed of analysis, less material consumption, and high throughput. The analyses range from simple tests on biological samples to sophisticated DNA and cell analysis in the low Reynolds numbers.

As the Reynolds number increases to intermediate levels (typically between 0.1 to 100) inertia becomes significant and ciliary motion can be replaced by reciprocal flapping motion. Mayfly nymphs (Figure 2a) are one example of flow generated within the intermediate Reynolds number range that occurs in nature. It typically exhibits a Reynolds number between 1 and 22 throughout its life span and utilizes seven pairs of external gill plates to pump water around its body to increase oxygen absorption and maintain its respiration. For a set of appendages to operate efficiently in different conditions (wide range of flow rates with different fluids properties), it must be effective in different ranges of Reynolds numbers (0.1-100). This regime, in which both the viscous and inertial effects are important, is less understood. A pump that is effective in viscous-dominated flows may no longer be effective in this transitional regime.

Researchers study various means of how fluid is transported in different bio-inspired models. Theories of natural locomotion in fluids utilizes low Reynolds number approximations, applicable to microorganisms, or assumptions of inviscid fluid dynamics, applicable to flying birds and fish (Table 1) (S. J. Lighthill 1975; S. Childress 1981; Dudley 2002). There are, however, an intermediate range of organisms, such as smaller insects and gastropods, for which characteristic Reynolds numbers lie in the range 0.1-100. In this range of intermediate Reynolds numbers, resolving the flow field is more complex.

These complexities arise because the use of either Stokes flow or inviscid theory is not clearly valid for intermediate Reynolds numbers ($0.1<Re<100$) and non-linear terms in the Navier Stokes equation are noticeable. The computational cost of studying the

intermediate Reynolds number regime is high. Modelling the influence of time-dependent geometries is also computationally cumbersome which adds to difficulties (J. F. Childress et al. 2002).

These complexities in resolving the flow field across intermediate Reynolds number motivates researchers to carry out experiments in this regime (A. T. Sensenig, Kiger, and Shultz 2009; A. J. Larson, Stover, and Keyes 2012; Khaderi, den Toonder, and Onck 2012). Moreover, application of such systems in novel chemical sensors (Vitko et al. 2004) and LOC devices are a strong motivation to explore fluid behavior in this regime. Pumping in microchannels has traditionally been conducted by downsizing the conventional syringe or micro pumps (Schilling, Kamholz, and Yager 2002; Laser and Santiago 2004) , or by implementing electro-magnetic fluid manipulation principles, as in electroosmotic and magneto-hydrodynamic devices.

As systems are continually decreased in size, there will be an increased demand to develop novel and efficient sampling platforms that are able to operate within a decreasing Reynolds number regime. Displacement micro pumps operate more efficiently in low Reynolds number. The nature of this pump causes the fluid to be delivered in discrete volumes, the size of which can be controlled by the volume of the chamber and the stroke length. One type of displacement micropump has a moving boundary exert pressure on the fluid, but with an aperiodic motion. These micro pumps have shown commercial success but are usually only effective with finite volumes of liquid. An example of such a device is an insulin delivery system marketed by Medtronic. There are many studies to explore fluid structure in solid/fluid interactions in sub-millimeter organisms (Whitesides 2006; Beebe,

Mensing, and Walker 2002; Burns et al. 1998). These studies can help improve future generations of distributed and autonomous chemical sensor networks, which often require an external convective current to achieve rapid and reliable performance.

For example, understanding the microcirculation pumping dynamics of mayfly nymphs represents a biological analog to such devices, operating within a comparable parametric space and requiring similar needs as an engineered autonomous micro-sensor platform. When faced with oxygen-poor conditions, the mayfly nymphs use their active gill array to generate a circulation current to enhance the momentum diffusion rate and maintain their metabolic requirements (Sapsford 2001; Lilienthal et al. 2001; Tang et al. 2002; Vitko et al. 2004).

Different Symmetry breaking Mechanism in nature

The Reynolds number determines many general features of a flow pattern, including the roles of viscous stress and pressure on a moving structure. There exist some general rules that relate kinematics to Reynolds numbers, both in theory and in surveys of the range of behaviors and structures seen in nature. According to the scallop theorem (Purcell 1977), time-reversible (or reciprocal) motion cannot generate a net propulsive force under creeping flow conditions. Put another way, a swimmer must deform in a way that is not invariant under time-reversal (e.g. one could readily discern a difference in the kinematic pattern when animated in forward- or reversed-time).

To effectively actuate fluids at low Reynolds numbers ($Re \ll 1$) an asymmetric motion is required. In nature, this is typically accomplished in ciliary beating through distinct kinematic shapes during the effective and recovery strokes (Khaderi, den Toonder, and Onck 2012). For example, each cilium in paramecium moves in asymmetric manner. It is relatively straight in the effective stroke, but it has a curvy shape during the recovery stroke. This results in more pumping during the effective stroke and a positive net flow. Moreover, when many cilia operate together, hydrodynamic interactions cause them to beat out-of-phase, leading to the formation of metachronal waves, and an enhanced fluid flow (Khaderi, den Toonder, and Onck 2012). In intermediate Reynolds number conditions ($Re \sim 1\text{-}100$), many insects use different mechanisms to generate flow around them. Mayfly nymphs, for example, introduce a distinctive feature which is the presence of 7 pairs of gill plates on the lateral dorsal region of the abdomen (Figure 2 a). The gill plates actively beat in a metachronal fashion to produce an external current that aids in the circulation of fresh oxygenated water and allows the mayfly to regulate

fluctuations in oxygen concentrations (Wingfield 1939; Eriksen and Mœur 1990; Bäumer, Pirow, and Paul 2000; Eriksen 1968).

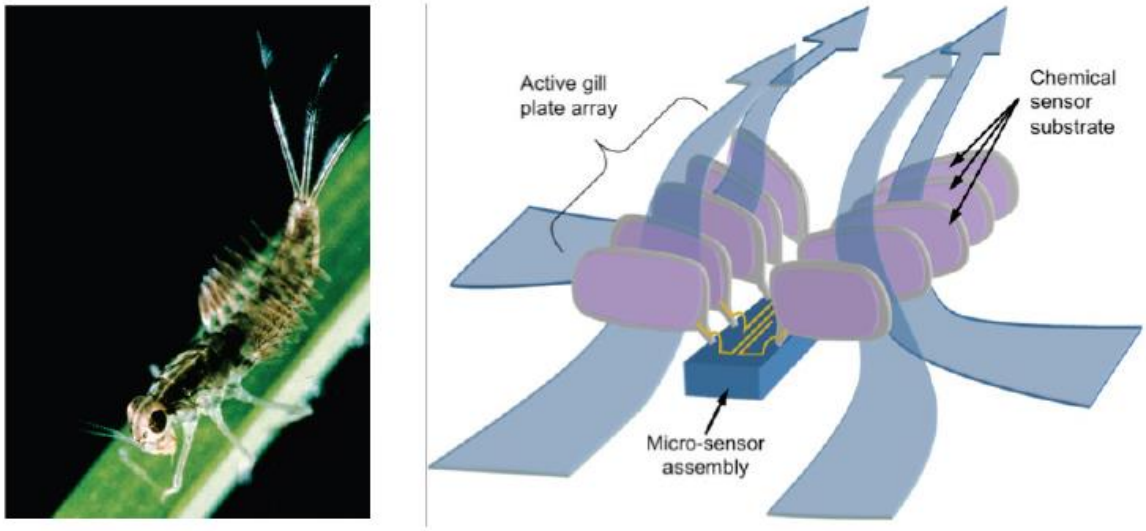

Figure 2. a) Ephemeroptera. Baetidae: Callibaetis ferrugineus nymph; photo by Mike Higgins, from the NABS Macroinvertebrates slide collection (www.benthos.org). b) Conceptual sketch of integrated biomimetic convective sensor

Three different nature-inspired mechanisms are investigated in this work within the intermediate Reynolds number regime. The results are used to demonstrate how breaking symmetry in intermediate level Reynold numbers affects the overall pumping performance of oscillating plate systems.

Firstly, in intermediate Reynolds numbers, Mayfly nymphs implement different stroke motion patterns to improve pumping. Faster effective stroke than recovery will result in finite net pumping (Gauger and Stark 2006; A. Sensenig, Kiger, and Shultz 2010). Secondly, gills in larger instars also acquired an intrinsic hinge that allows passive asymmetric movement between half strokes. Distinct effective and recovery stroke kinematics will result in finite net pumping. This is also seen in cilia (Low Reynolds numbers) which are almost straight in effective strokes, but they bend in recovery strokes (Khaderi, Den Toonder, and Onck 2011). Thirdly, Mayfly nymphs live under

the water and circulating oxygenated water to its body by applying phase lag between adjacent gills in oscillating seven pairs of gills. Time delay between adjacent gills will produce metachronal wave, and therefore it creates non-reciprocal motion in the array. Previous three-dimensional study of mayfly examined the effect of symmetric actuation and metachronal motion (implementing phase lag between adjacent gills) on the pumping in the array of five gills (Mary Larson et. al. 2012). They found that among four different case studies optimum pumping occurs at metachronal phase lag of $\Delta\theta_i = 90$ and the energy dissipation is minimal for $\Delta\theta_i = 0$. Senssing et al. 2010 studied the oscillating array of gill plates of the mayfly nymph of the species *Centroptilum triangulifer*. Their results indicate that flow within the mayfly nymph's gill array at all sizes is produced by ring vortices generated at the margins of each moving gill, and that the metachronal phasing of the gill kinematics produces a time-dependent array of vortices that was termed a 'phased vortex pump'. Circulation is calculated by integrating a vorticity field over a closed area. Stronger circulations tend to be more energetic and therefore could be related to higher momentum transfer from solid boundaries (Lamb 1932). To further explore the effect of metachronal motion in the array and examining different asymmetric input actuation patterns, current study carried out in a two-dimensional channel. In the preliminary experiments, to fully understand the physics behind pumping in an array of oscillating plates, we primarily studied a single rigid/flexible plate in a channel. In nature, there are several examples of different species using a single appendage for swimming and pumping.

For example, Jellyfish represents well-studied class of propulsion within the intermediate Reynolds number regime. The power stroke in jellyfish is provided by fast muscle contraction around the edges of their bell which is exerts momentum to the fluid. The contraction forces out the water stored inside the bell. The effective stroke is followed by a slow retraction of appendages for the recovery stroke (Nawroth and Dabiri 2014). The scallop is another example: it opens its shell slowly and closes it fast, squirting out water to provide thrust (Manuel and Dadswell 1993).

In the intermediate Reynolds numbers, momentum transfer from solid boundaries to the fluid occurs mainly through advection of vorticities near solid boundaries in both swimming and pumping. In inertia-driven flow, optimal vortex formation will serve as a relevant criteria to improve fluid propulsion in swimmers (Dabiri et al. 2010). For example, the manner that fish move head to tail will give rise to circulation around its body which is necessary in small viscosity flows (such as water) to produce a forward force by hydrodynamic reactions (Gray and Hancock 1955).

In the second phase of experiments, 2D pumping in the array of multiple plates are examined. The array of oscillating plates is placed in a channel to measure how increased asymmetry and Reynolds number would affect the net pumping. Particle image velocimetry (PIV) technique is used to calculate velocity vectors in 2D channel flow. One-way flexibility and the time delay are introduced to the adjacent rigid plates to study the effect of non-reciprocal motions on a pumping. One-way flexibility will produce non-reciprocal motion in which plates are rigid in the effective stroke but bend in the recovery stroke. Non-reciprocal motion of the flexible plates will generate more pumping in the forward stroke for all flow conditions. In the case of metachronal input

actuation, hydrodynamic interaction between delayed adjacent gills will result in a non-reciprocal motion and a finite pumping (M. Larson et al. 2014; A. Sensenig, Kiger, and Shultz 2010).

In the next section I will define the problem definition to examine different symmetry breaking mechanisms in nature.

Chapter 2: Problem definition and Experimental setup

Problem definition for single plate experiments

We perform the experiments in a channel of length L, height H, containing a single rigid plate. (Figure 3)

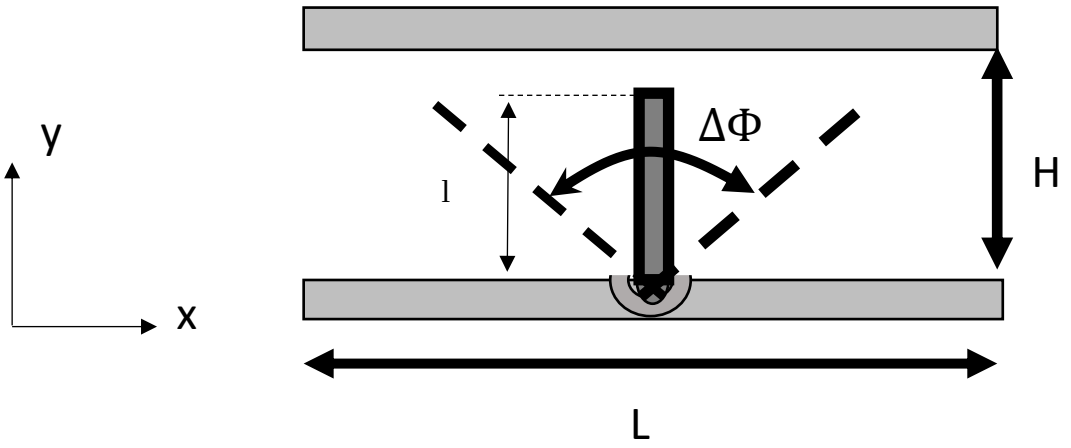

Figure 3.Schematic of problem geometry

A position-base input wave which varies in time is used for actuation. The effect of different asymmetric kinematics on pumping performance of rigid plates are investigated. Four different patterns are generated with the same feature: namely having an effective stroke that is more rapid than the opposing recovery stroke, as depicted in Figure 4.

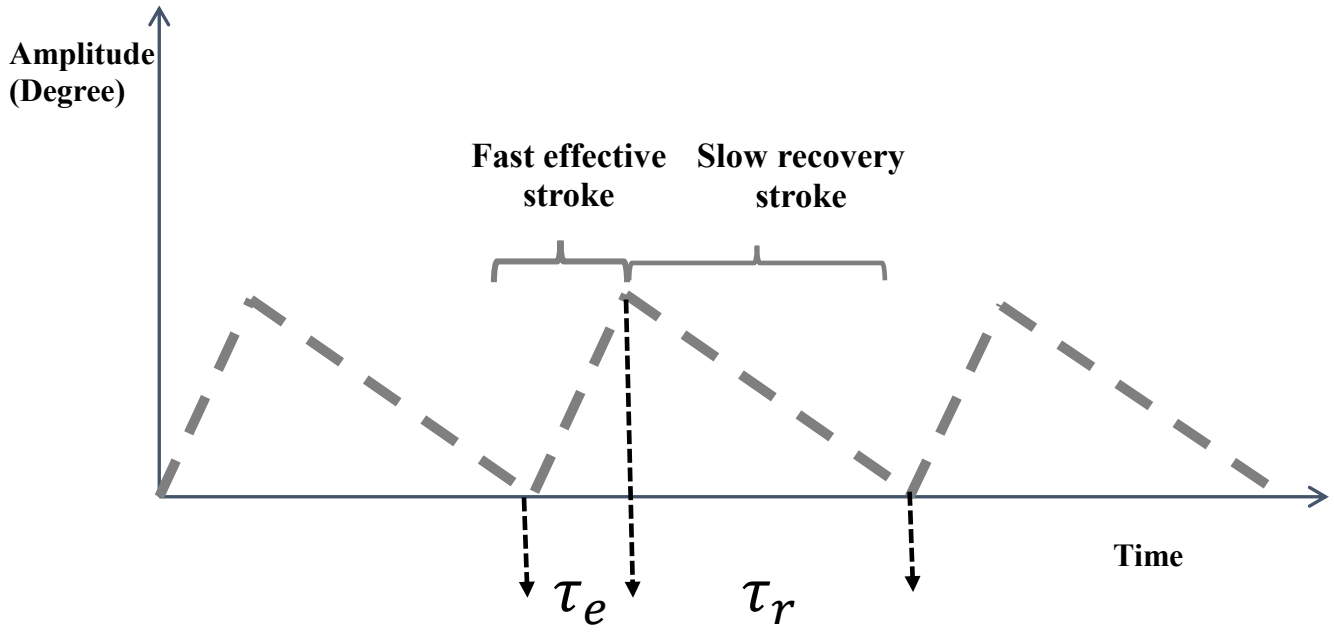

Figure 4.Schematic of effective and recovery stroke

To more readily parameterize the degree of asymmetric motion, the so-called kinematic asymmetry parameter is defined in eq.1.(Gauger and Stark 2006)

$$\epsilon_k = \frac{\tau_r - \tau_e}{\tau_r + \tau_e} = \frac{f_e - f_r}{f_e + f_r} \quad (1)$$

Due to the asymmetric motion, the Reynolds number parameterizing the effective stroke is likewise higher than during recovery stroke because of asymmetry of input kinematics. Asymmetry parameter (ϵ_k) is the measure of asymmetry in the given triangle input wave. We have found the relationship of (ϵ_k) to effective Reynolds number and recovery Reynolds number.

$$\Re_{effective} = \frac{{L_f}^2 * f_e}{\vartheta}\Delta\Phi \gg \Re_{recovery} = \frac{{L_f}^2 * f_r}{\vartheta}\Delta\Phi \; --\!\!\rightarrow R = \frac{\Re_{effective}}{\Re_{recovery}}$$

$$= \frac{f_e}{f_r} \quad (2)$$

From 1 and 2 →

$$R = \frac{1 + \epsilon_k}{1 - \epsilon_k} \; (3)$$

Here f_e and f_r are effective frequencies associated with the half strokes. Equation 3 demonstrates that the ratio between the Reynolds number in effective and recovery stroke is related to the asymmetry parameter.

In the current work, a "one-way" flexibility is introduced by joining two segments of the plate with a flexible tape, allowing the plate to be straight in effective stroke, but bend freely during the recovery stroke (see Figure 5).

In addition to allowing for an asymmetric beating pattern, permitting the geometry of the gills to change during the effective and recovery stroke can accentuate the asymmetry and potential lead to increased effectiveness. A simple and passive means to permit such conformal changes is to utilize a one-way elastic hinge, as illustrated in Figure 5. The idea of the elastic one-way hinge allows us to passively keep the jointed plate straight during the effective stroke to maximize drag and pumping in the favorable direction, but to allow bending in the recovery stroke for minimal pumping in the reverse direction.

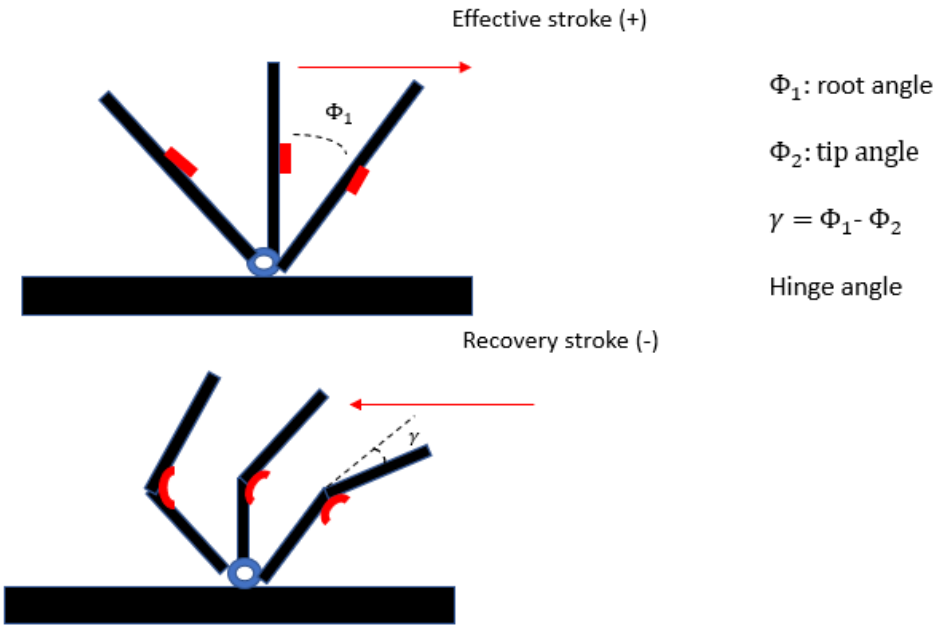

Figure 5. Demonstration of different angles of a plate in the presence of one-way elastic hinge

Single flexible plate consists of two rigid segments of acrylic. Segments are attached via single-sided adhesive Kapton tape manufactured by Ted Pella company. This tape has tensile strength of 30 (lb⁄in) and elongation is >40%.

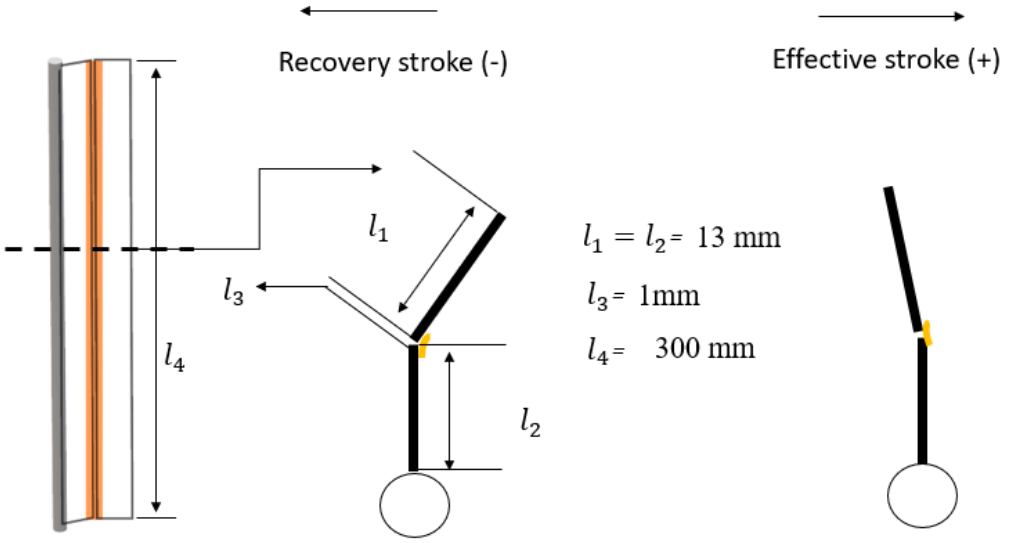

Figure 6. Schematic of flexible plate

In Figure 6, 2 segments of thin acrylic sheet (13x300x1.6 mm) are attached via elastic hinge which will allow the appendage to bend in recovery stroke. Segments are attached to 10 mm diameter acrylic rods (Figure 6).

Calculations

To characterize net pumping that occurs over one beat cycle, we introduce a parameter called the pumping performance Π. This parameter is a space and time averaged horizontal velocity that provides a measure of the net mean flow produced by the pumping action. For planar flows, it can be calculated from two-dimensional particle image velocimetry (PIV) measurements, as described below.

Pumping Performance Π:

First, the time-averaged horizontal velocity field, $U_{avg,}$ of all PIV images is calculated

$$U_{avg}(x.y) = \frac{1}{T}\int_{t=0}^{t=T} u(x.y.t)\,dt = \frac{1}{N}\sum_{i=1}^{N} u_i(x.y)\,dn \quad (4)$$

where, $T=1/f$ is the period of the oscillation cycle, N is number of PIV images (typically ~500), and u_i is instantaneous velocity within the discrete i_{th}PIV image, x is the streamwise direction and y is the wall-normal direction.

The streamwise-averaged velocity profile, $U_p(y)$, gives a measure of the average velocity distribution with respect to channel height, and is calculated by averaging $U_{ave}(x.y)$ along the channel.

$$U_p(y) = \ velocity\ distribution\ along\ the\ channel\ height$$

$$= \frac{1}{L}\int_{x=0}^{x=L} U_{ave}(x.y)dx \quad (5)$$

Finally, the pumping performance is defined as the cross-sectional average velocity by integrating U_p across the channel height.

$$Pumping\ performance\ \Pi = \frac{1}{H}\int_{x=0}^{y=H} U_p(y)dy \quad (6)$$

An instantaneous Pumping performance can also be calculated at each specific phase which represents the net volumetric flow pumped at each phase.

$$U_{(y.t)} = net\ horizental\ velocity\ along\ the\ channel = \frac{1}{L}\int_{x=0}^{x=L} u(x.y.t)dx \quad (7)$$

$$\Pi_t = \frac{1}{H}\int_{y=0}^{y=H} U_{(y.t)}dy \quad (8)$$

In which Π_t is instantaneous pumping performance.

Experimental setup and 2D flow

A programmable robotic oscillating plate array was designed to permit a systematic measure of pumping performance for a 2D flow in a channel. The robot can be actuated with arbitrary input signals such as sinusoidal or triangle waves with different asymmetry parameters. The plates and channel were designed with a large aspect ratio to help insure that the flow remains two-dimensional. A ratio of 12:1 was used for the plates (28 mm x 300 mm), and they were embedded in a channel with a wall separation of H = 38 mm. Despite this large aspect ratio, the flow would ultimately exhibit three-dimensional behavior at sufficiently large Reynolds numbers. In the Appendix B, proof of 2D flow in the experiments is tabulated.

In Figure 7 pumping performance is calculated at three different cross sections in the channel (Inflow, outflow, and the entire channel).

Pumping performance values calculated by integrating over ~1cm of beginning of the channel (black marker) over entire channel (red markers) , and at the 1cm of end of the channel (blue markers). 3D effects are within 7% of overall pumping performance. This is the extreme case in which effective stroke Reynolds number ~28. As it seen average discrepancies between following measurements is less than 5% and 3D effects are higher in the effective stroke (Figure 7).

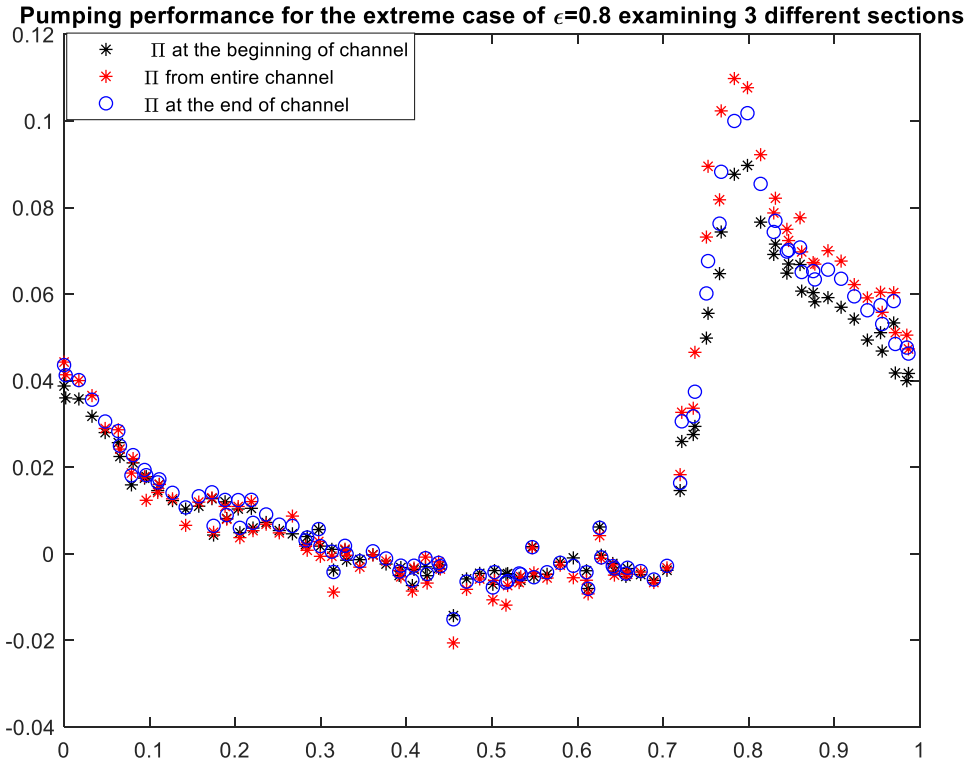

Figure 7. Examining the 3D effects for ε=0.8

In addition to using asymmetric actuation kinematics, passive asymmetry can be introduced into the plate motion by creating plates with asymmetric flexibility. By this means, even with symmetric input actuation, the plate will bend more readily

when executing motion in a given direction, leading to asymmetric geometries throughout the cycle (Figure 5).

Experiments were carried out in an aquarium with overall dimensions of (260 x 310 x 510 mm^3), filled with mineral oil (viscosity of ~ 60 Cst) or glycerin (viscosity of ~ 600 Cst), permitting an operational range of Reynolds number from 0.1 to 100. Viscosity is calculated several times by using Cannon viscometer size 200 (for oil) and 350 (for glycerin). Averaging the three different measurements indicate ~60 cst for oil and ~ 600 cst for glycerin.

The channel itself was constructed from acrylic sheets, giving dimensions of 125mm x 200 mm, and mounted inside of the tank such that the ends permit the pumped flow to circulate within the bulk of the tank. The array of five plates is placed in an aquarium tank in which the dimension reflected in the figure 8. Channel length is 250mm and its height is ~35mm. Plates length is ~28mm and the spacing between plates is 40mm.

L: Channel length =360 mm l: Gill length=28mm s: Spacing = 40 mm H: Channel height=35mm

HH: aquarium tank's height= 310 mm LL: aquarium tank's length= 510 mm

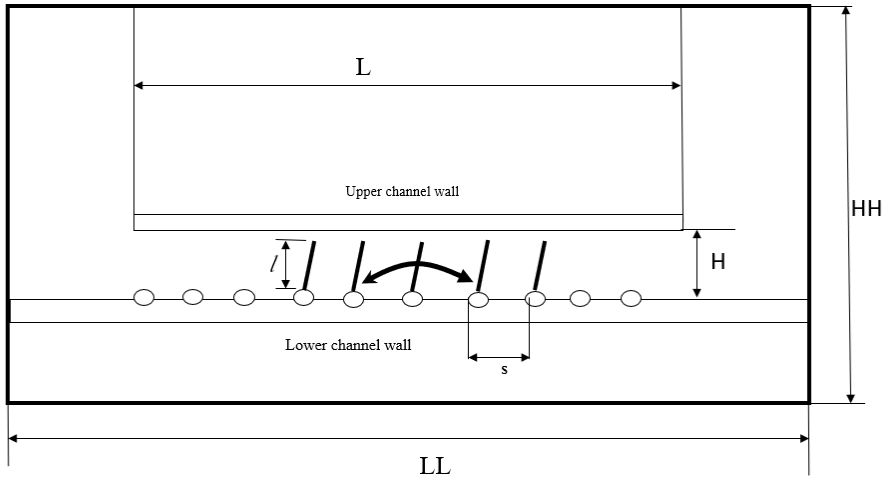

Figure 8. Schematic and dimension of a plate in the channel

The actuation plates were constructed from thin acrylic sheet (~ 1.6 mm thickness) and attached to 10 mm diameter acrylic rods. The "lower" wall of the channel was constructed from a thick acrylic plate (3/8" thickness) and served as the wall to which the actuated plates were attached. The wall was machined with cylindrical grooves to permit recessing of the actuation rods by one rod radius to provide a conformal guide and pivot location. Once in place, the acrylic rods were coupled to DC motor shafts by means of a flexure coupling and a gearbox. The gearbox included two bevel gears to transmit power to vertical shafts (Figure 10). An absolute magnetic shaft encoder (US Digital MA3) was coupled to the motor shaft to monitor shaft position. A position-based PID (proportional–integral–derivative) feedback controller (Pololu JRK 21v3) was used to minimize errors between the input signal and actuation. Figure 9 demonstrates the discrepancies between input signal sensed at the feedback

controllers input and the position sensor output. There is a slight hysteresis at the zero velocity points that could not be tuned from the system. In all cases the observed r.m.s. discrepancy is less than 3%, with a maximum deviation of less than 5%.

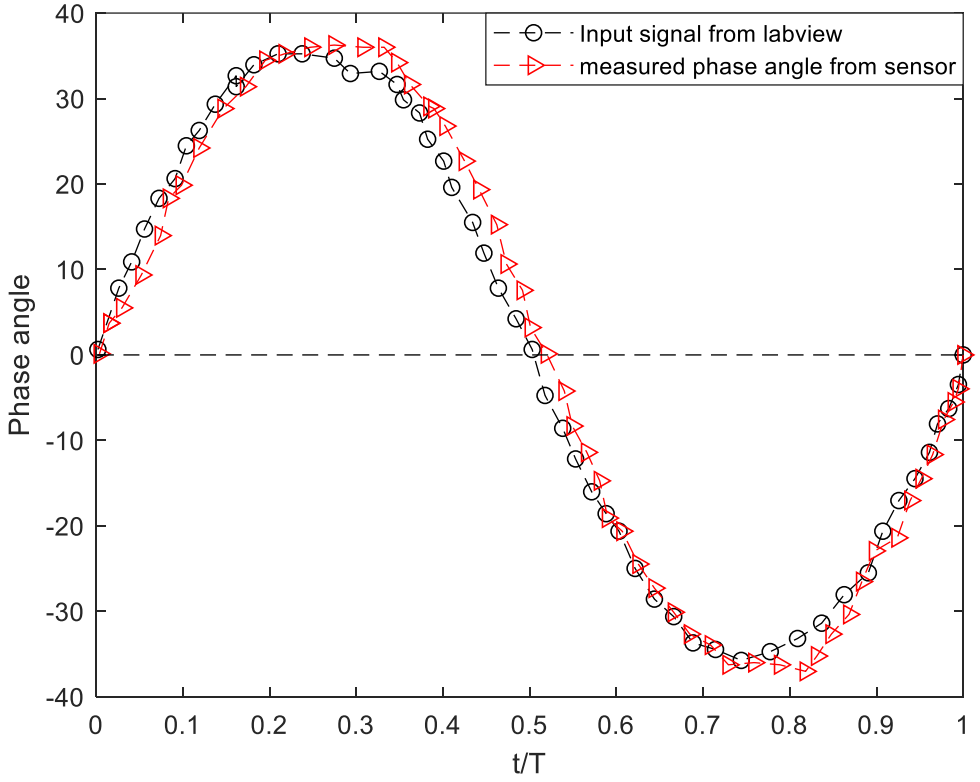

Figure 9. Input signals from LabVIEW and output signals from the sensor over a typical full cycle

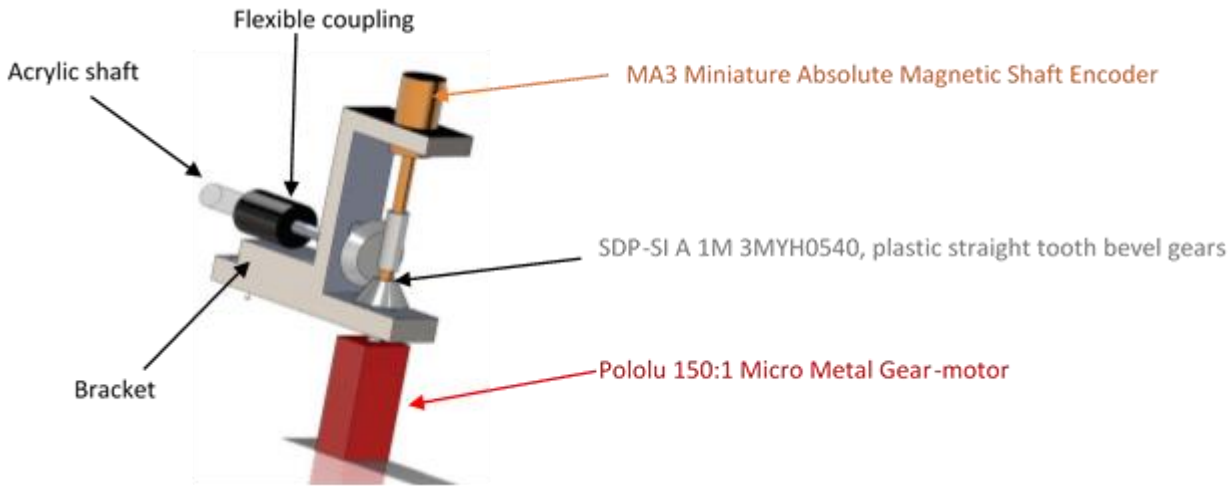

Figure 10.Miniature gearbox and its components

A standard particle image velocimetry (PIV) technique was used to obtain the velocity field around oscillating plates, as shown schematically in Figure 11.

A Litron nano PIV Nd:Yag laser system was used to generate a 532 nm wavelength light sheet. The laser beam (R~3.5mm) was converted to a 30cm wide laser sheet using series of optics consisting of the -12.5mm focal length MgF2 coated cylindrical lens and two mirrors. Light sheet thickness measured to be (~1 mm). The laser sheet illuminated a horizontal slice at the center of the tank (Figure 11). Two LaVision Imager Pro X 4M cameras (2048x2048 pixels) were used with overlapping co-planar fields of view. Cameras were equipped with two 200mm Nikon lenses with the aperture set at f/5.6. The cameras were positioned approximately 2 meters from the tank to record images illuminated by the laser sheet. The typical camera field of view was approximately $12 * 12\ cm^2$ for each camera. Silver-coated glass spheres (Potters industries) with an average diameter 10 ± 5 μm were used as particle tracers.

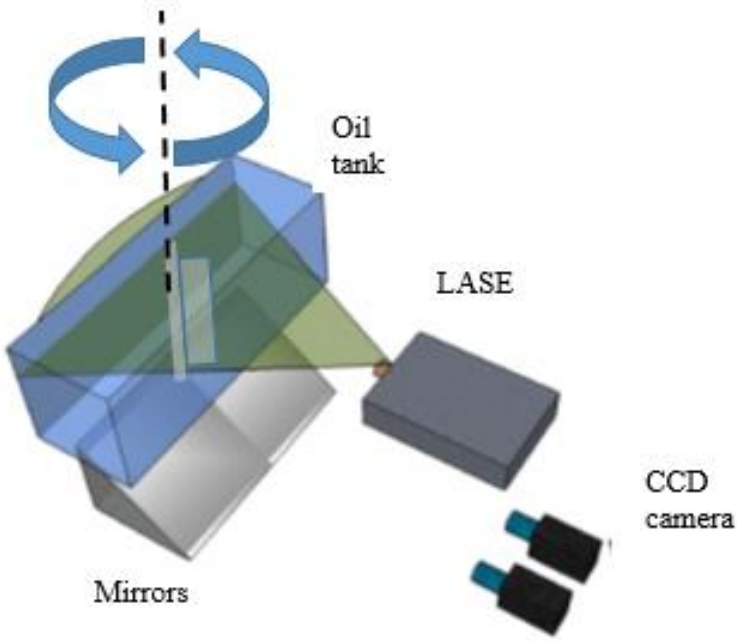

Figure 11. Schematic of experimental setup

The velocity field is obtained using a standard multi-pass algorithm and sequential cross-correlation using a commercial processing software (DaVis v8.20). The initial interrogation pass is set to use an area of 96x96 pixels and an overlap of 50%. The vectors from this pass then serve as an estimate for two following passes of a smaller 24 x 24 pixel windows with a 50% overlap.

Uncertainty

To calculate uncertainty of experiments we assume that maximum uncertainty occurs when plate passes the $\Phi = 0$ in the effective stroke (t/T = 0.25). It is assumed that when a plate passes from $\Phi = 0$ it exhibits the maximum velocity (It is far from two stationary beginning and end) and the uncertainty is higher:

$$\Delta U_i = \frac{t\sigma_u}{\sqrt{N}} \quad (9)$$

Where σ_u is the standard deviation of the ensemble of *N* samples of the velocity, and *t* is the scaling factor for the student-t distribution. For this analysis, *N* = 10, and *t* = 2.28 for a two-sided 95% confidence interval.

The pumping performance is calculated as follows:

$$\Pi = \frac{1}{LH}\int_{y=0}^{y=L}\int_{x=0}^{y=H} U_{ave}(x.y)dxdy \quad (10)$$

$$\Pi = \frac{1}{LH}\int_{y=0}^{y=L}\int_{x=0}^{y=H} U_{ave}(x.y)dxdy = \frac{1}{N_x N_y}\sum_{i=1}^{N_x}\sum_{j=1}^{N_y} U_{ave}(x.y)\,\delta x\delta y \quad (11)$$

The propagation of uncertainty of time-averaged field in the pumping performance will be:

$$\Delta\Pi_u^2 = \frac{1}{N_x}\frac{1}{N_y}\sum\nolimits_1^{N1}\sum_1^{N2}(\Pi * \delta x_i \delta x_j)^2\left[\left(\frac{\Delta U_{avg}}{\Pi}\right)^2 + \left(\frac{\Delta\delta x_i}{\delta_{xi}}\right)^2 + \left(\frac{\Delta\delta x_j}{\delta_{xj}}\right)^2\right] \quad (12)$$

In which $\Delta\delta x_i$ is the uncertainty in the grid spacing and negligibly small ~0.002. The uncertainty of pumping performance for high frequency actuation (f=0.88 HZ) in single flexible plate is ~%0.7. Uncertainty of other cases are tabulated in the table 2.

Dissipation uncertainty propagation:

Foucaut and Stansislas (2002) explored the errors in velocity gradients from PIV methods and reported specifically on results for using the central difference schemes that are used in this thesis to calculate derivatives used in dissipation rate equation. They introduced truncation error and noise error and concluded that truncation error is 15% of noise error and can be neglected.

The uncertainty in the dissipation for current 2D experiments at each point at the surface is:

$$\Delta\varphi^2 = \mu\left[(4\frac{\partial U}{\partial x})^2(\Delta\frac{\partial U}{\partial x})^2 + (4\frac{\partial V}{\partial y})^2(\Delta\frac{\partial V}{\partial y})^2 + 4(\frac{\partial V}{\partial x} + \frac{\partial U}{\partial y})^2(\Delta\frac{\partial V}{\partial x})^2 + 4(\frac{\partial V}{\partial x} + \frac{\partial U}{\partial y})^2(\Delta\frac{\partial U}{\partial y})^2\right] \quad (13)$$

To calculate total dissipation, as previously seen, time averaged dissipation is summed over x and y direction:

$$\varphi_{total} = \sum_{i=1}^{N_x} \sum_{j=1}^{N_y} \varphi_{ij}\, \delta_x \delta_y \quad (14)$$

$$N_x = Number\ of\ values\ in\ the\ x\ direction$$

$$N_y = Number\ of\ values\ in\ the\ y\ direction$$

$$\varphi_{total-avg} = \frac{1}{100} \sum_{i=1}^{N=100} \varphi_{total} \quad (15)$$

The propagation of uncertainties will result in:

$$\Delta\varphi_{total}{}^2 = \sum_{i=1}^{N_x} \sum_{j=1}^{N_y} (\varphi_{ij} \delta_x \delta_y)^2 \left[\left(\frac{\Delta\varphi_{ij}}{\varphi_{ij}}\right)^2 + \left(\frac{\Delta\delta x_i}{\delta_{xi}}\right)^2 + \left(\frac{\Delta\delta x_j}{\delta_{xj}}\right)^2 \right] \quad (16)$$

$$\Delta\varphi_{total-avg} = \frac{1}{100} \sum_{i=1}^{N=100} \Delta\varphi_{total} \quad (17)$$

Table 2.Uncertainties for extreme cases for pumping performance an the dissipation rate of a single plate and an array of five plates

Case	ΔU_i	$\Delta\Pi$	$\Delta\varphi$
1.TsR30	0.03	0.9×10^{-5}	0.009
2.TAR30	0.067	3.66×10^{-5}	0.004
3.SAf90	0.018	0.0007	0.0038
4. FF	0.01	1.5×10^{-4}	0.00013

First three cases in the table 2 have name tags which are introduced later in chapter 4 table 6. Name tag for case#4 is introduced in Chapter#3 table 2.

All the uncertainties in the Table 2 are dimensionless. This propagation yielded uncertainties of ~±1% of the average of the total flow in and out of the control

volume and uncertainties of approximately ~ ±2% of the total, cycle-averaged dissipation. The uncertainty is the highest for SAF90 which is ~±4%. Uncertainty of dissipation rate for a single flexible plate is ~%1. The higher uncertainty in dissipation rate is due to the higher uncertainty propagation in the squared velocity gradients.

Chapter 3: Results for oscillating single plate in a channel

In this chapter we systematically studied different symmetry breaking mechanisms to observe their effect on pumping in two different Reynolds number. We started from the symmetrical sine actuation of rigid plate in the channel. Triangle waves with different asymmetry parameter were studied and the effect of increased asymmetry parameter on a flow structure and pumping is tabulated. One-way flexibility is added to the rigid gill which produce non-reciprocal motion and signifies more pumping in the effective stroke.

Reciprocal oscillating sine motion of a single rigid plate in a channel

The first series of measurements examine the role of asymmetric actuation kinematics of a rigid plate at two different Reynolds numbers (Re = 0.6 and 6), utilizing constant velocity triangle waves for the angular actuation kinematics. In all cases, the more rapid actuation will be denoted as the "effective" stroke and will be rotated in the clockwise direction, while the "recovery" stroke will follow in the counter-clockwise direction to complete the cycle. The case of temporal asymmetry will be presented and discussed first, and then compared to the relative influence of flexibility on pumping. Snapshots of the flow at four different times within the cycle (t/T = 0, T/4, T/2 and 3*T/4), along with the time-averaged flow, are shown for the symmetric actuation case in Figure 12. These figures show the velocity magnitude along with the streamlines (left column), and the out-of-plane vorticity field (right column). Typical features common to the motion are exemplified by a dominant counter-clockwise circulation (positive vorticity) generated at the plate tip during effective stroke (Figure 12a, f; t/T = 0). The motion of the tip passing close to the wall also generates

a high shear region of negative vorticity on the upper wall boundary. At the end of the effective stroke (Figure 12b, g; $t/T = 0.25$), the plate is at rest and the strong positive vortex generated previously during the effective stroke has dramatically reduced in strength, while a negative region of vorticity has started to be produced along the plate surface and tip. The recovery stroke mirrors the effective stroke in terms of the generation, advection and dissipation of vorticity with the complementary strength and positioning.

The time-averaged vorticity field for the symmetric case features two dominant recirculation regions symmetrically placed on either side of the plate root position (Figure 12e, j). The vorticity field reveals that this flow is produced by six distinct regions of vorticity, with the two largest in the mid-region of the channel, flanked by four weaker regions localized near the wall boundary. Calculations of the net pumped flow show that the net pumping is effectively zero (the calculated mean value is order of magnitude lower than uncertainty of the measurement), as one would expect for this case.

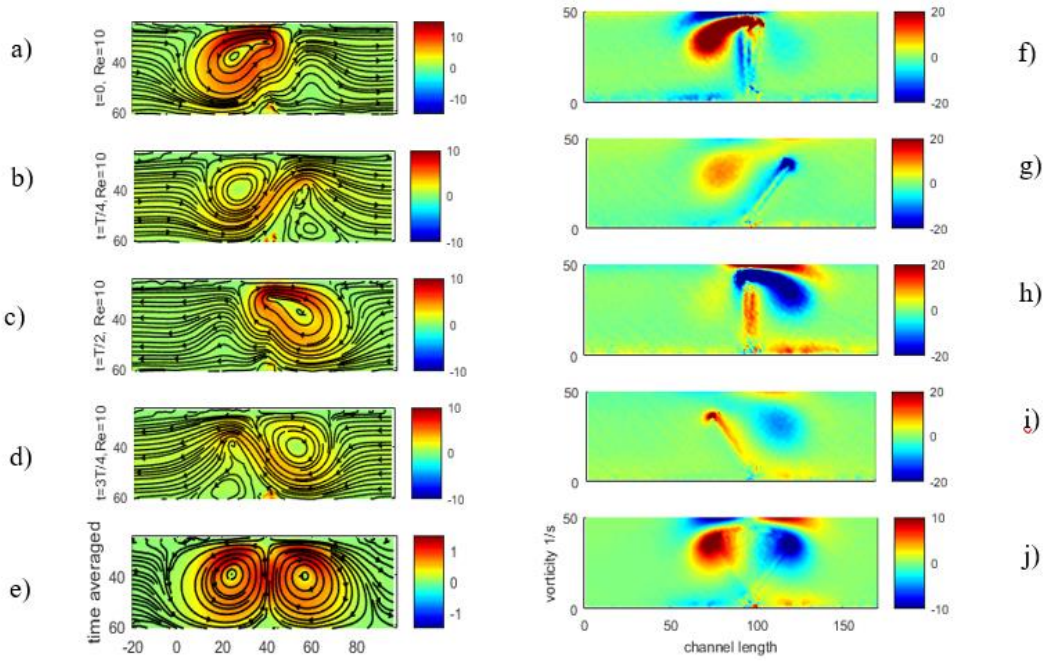

Figure 12.1) Streamlines of fluid motion of oscillating symmetric sine wave actuation (f=0.6 Hz, A=72 degrees) of a a) Streamlines in a rigid plate for a) t=0, b)t=T/4, c)t=T/2, d)t =3*T/4, and e) time-averaged case 2) Vorticity field for f) t=0, g)t=T/4, h)t=T/2, i)t =3*T/4, and j) time-averaged case

Asymmetric reciprocal triangle cases

Eight different experiment cases are carried out in oil and glycerin with viscosities v ~ 60 Cst and 600 Cst, giving a variation of an order of magnitude in the Reynolds number for identical kinematics, and are tabulated in Table 3.

The Reynolds number is 6 for the experiments in oil and 0.6 for the experiments in the glycerin. The half-stroke Reynolds numbers ranged from a minimum of $\Re_{recovery} = 0.4$ to a maximum of $\Re_{effective} = 28$ in these experiments.

Labels listed in Table 3 are to provide a shorthand reference to the different cases. "R" stands for rigid, "H" stands for high, "L" stands for low.

Table 3.Test conditions for asymmetric triangle input actuation

Label	ϵ_k	ϵ_o	$\Re_{effective}$	$\Re_{recovery}$	Re
RH-1	0	0	6	6	6
RH-2	0.4	0.3	17	7	6
RH-3	0.6	0.6	20	5	6
RH-4	0.8	0.7	28	4	6
RL-1	0	0	0.6	0.6	0.6
RL-2	0.4	0.3	1.7	0.7	0.6
RL-3	0.6	0.6	2	0.5	0.6
RL-4	0.8	0.7	2.8	0.4	0.6

Experimental input kinematics can be acquired by tracking the gill tip from PIV images and it is shown in ϵ_o column. Tracking will provide the position of plate at specific phases. It is done through marking a gill tip with illuminating tracer particles and tracking it throughout the cycle. In Figure 13, the angle of plate is measured by tracking the tip of plate from the PIV images.

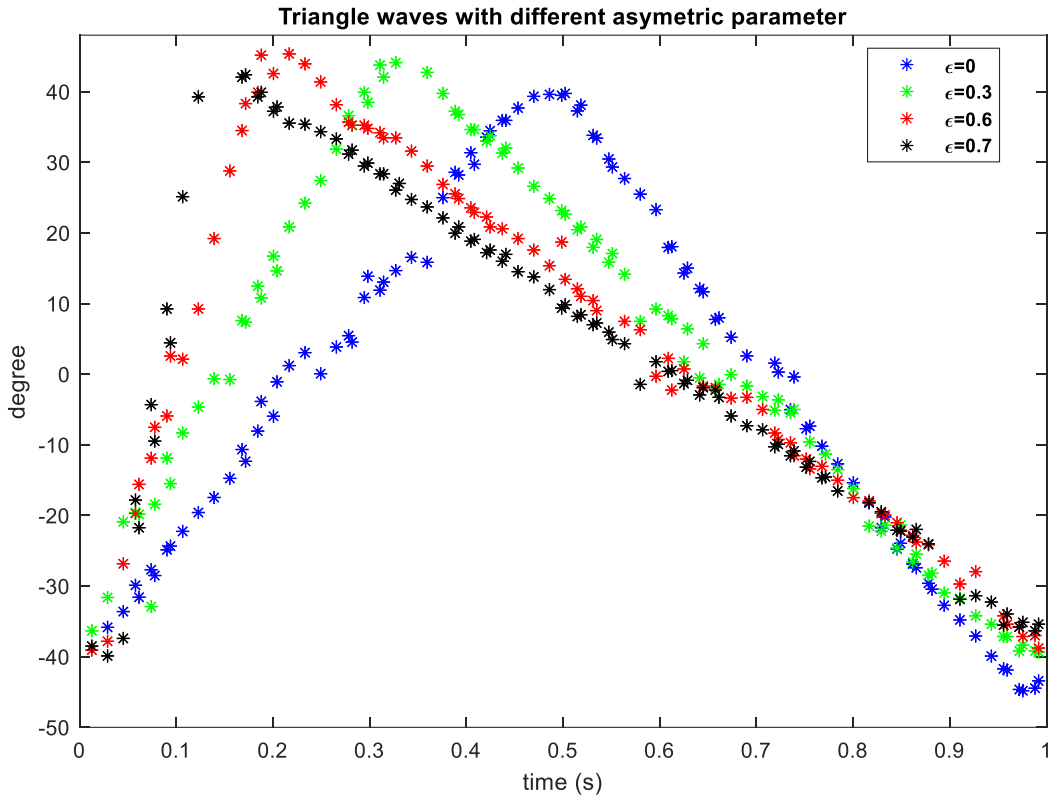

Figure 13.Phase angles of a gill from PIV images by using tracking method of plate's tip for Reynolds number~6

In Figure 13, RH-1 ($\varepsilon = 0$) is the symmetric case with the triangle wave input which will generate no pumping within uncertainty of experiments, like the sinusoidal actuation input signal that is shown in Figure 12. RH-2 is slightly asymmetric, in which the effective stroke duration is shorter than the recovery stroke. RH-3, and RH-4 are more asymmetric in which effective stroke is approximately 2.5 and 4 times faster than recovery stroke, respectively. The prescribed input waveforms specified $\varepsilon = 0; 0.4; 0.8$, slightly differed from the observed experimental asymmetry parameter (ϵ_o) in Figure 13. This is due to the response of the feedback control

system's in ability to match exactly the rapid transitions that occurred at stroke reversal.

Following the baseline symmetric actuation case shown above, experiments were performed at four different values of the asymmetry parameters ($\varepsilon = 0;\ 0.4;\ 0.6;$ and 0.8) and at two different Reynolds numbers of Re = $fl^2\Delta\phi/\nu$ = 0.6 and 6. The first set of experiments were carried out in glycerin with Re = 0.6. Using the given set of asymmetry parameters, the Reynolds number during the effective stroke ranged from $0.6 < \mathrm{Re}_{eff} < 2.8$, while during recovery stroke the values were bounded by $0.06 < \mathrm{Re}_{rec} < 0.6$. Instantaneous pumping performance Π_t is calculated throughout the beat cycle and it is shown for one period in Figure 14.

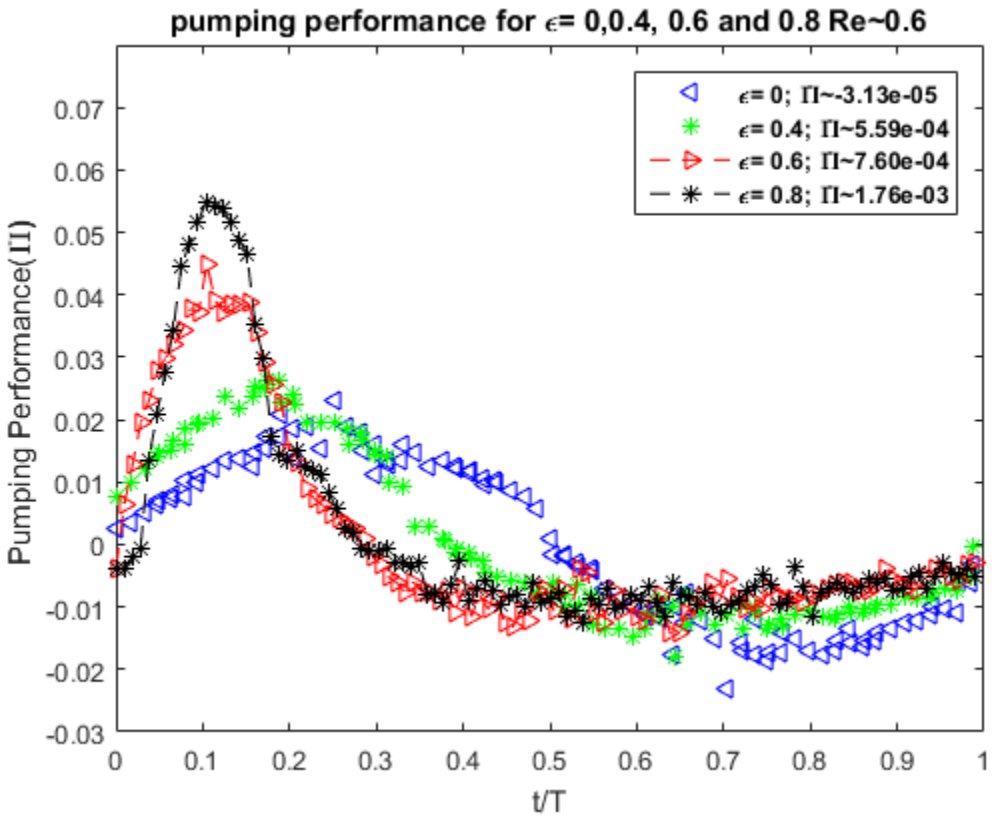

Figure 14. Pumping performance at each phase in one beat period for experiments in glycerin (Re~0.6)

Figure 14 demonstrates a sharp rise and fall in pumping performance curve. Horizontal component of velocity is normalized by $U_{normalized}$ which is the tip velocity in a beat cycle and is constructed by using gill length, beat frequency, and amplitude, $U_{normalized} = 2 * f * l * \Delta\Phi$ in a cycle.

In the limit of zero Reynolds number, reciprocal motion of the plate will result in a zero net pumping according to scallop theorem, even if there is a difference in velocity between the effective and recovery stroke. As the Reynolds number increases in Figure 14 to Re~0.6, a noticeable momentum transfer occurs from the moving plate during the effective stroke, resulting in a sharp rise in pumping performance curve. Increased values of ε produce maxima in pumping performance earlier in the cycle and attain higher magnitudes. As the plate gradually returns during the recovery stroke, there is a corresponding sharp decay in pumping performance curve. The experiments performed at the higher Reynolds number condition (Re~6) demonstrates similar qualitative trends with few discrepancies from low Reynolds number experiments, as shown in Figure 15.

The instantaneous peak pumping performance achieved near the end of the effective stroke for the Re = 6 conditions (Figure 15) is approximately twice the value attained at Re = 0.6 (Figure 14) due to higher inertia of latter experiments. The impact on the net pumping performance is even more dramatic, with values are approximately order of magnitude higher for the Re = 6 case, which emphasizes the strong and nonlinear role of inertia in these experiments to improve pumping.

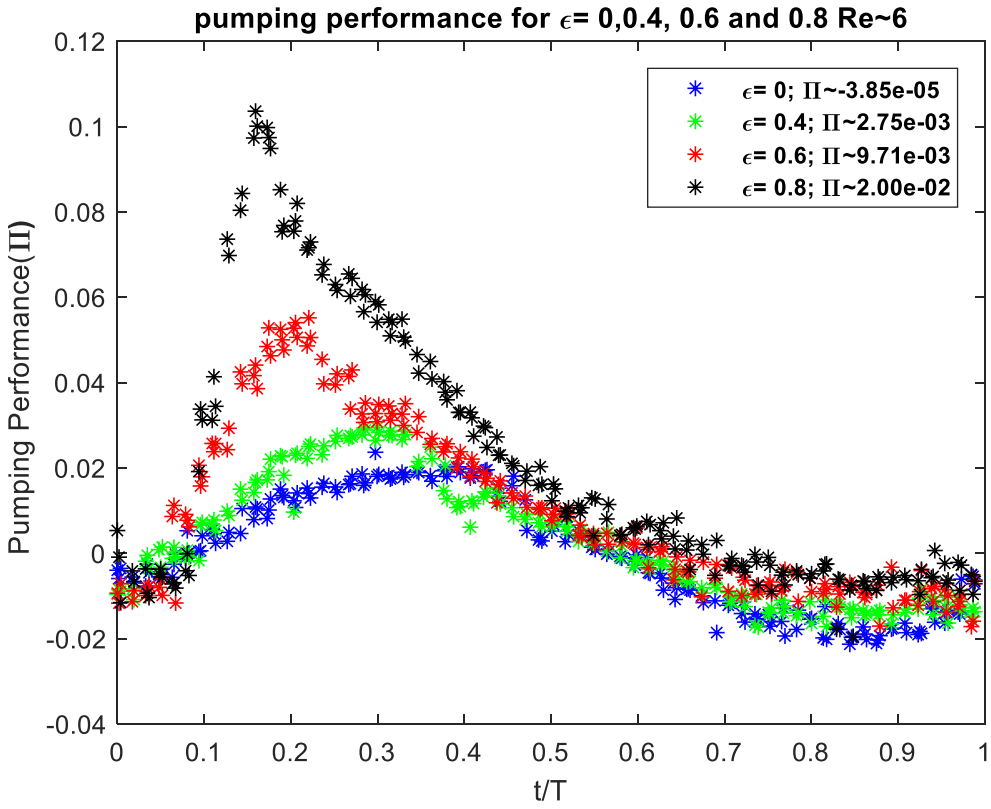

Figure 15. Pumping performance at each phase in one beat period for experiments in oil (Re~ 6)

More gradual rise and fall of instantaneous pumping performance demonstrate noticeable unsteadiness and non-linearities in the flow field.

In the Figure 16 ensemble averaged vorticity field at four different phases throughout the cycle is shown. Two first phases with strong CCW vortices are in the effective stroke (Figure 16. a, b) and (Figure 16. c, d) is in the recovery stroke.

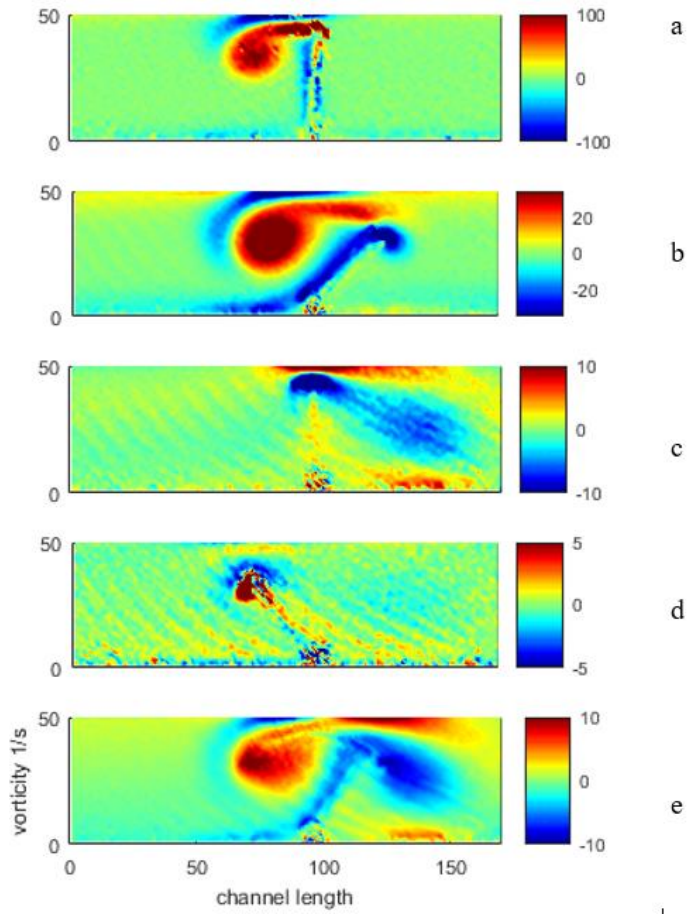

Figure 16. Ensemble_averaged vorticity fields for RH-4 (a-e) and time averaged vorticity field (e) a) ensemble-averaged velocity field at Φ=0 in the effective stroke. b) ensemble-averaged velocity field at t=T/4 at the end of effective stroke. c) ensemble-average velocity field at t=T/2 in recovery stroke. d) ensemble-averaged velocity field at t=3T/4 at the end of recovery stroke

In Figure 16 we can clearly conclude that the vortex that is formed during the effective stroke has a much higher instantaneous circulation value, and persists past the end of the stroke for longer, enabling it to induce a stronger current in that stroke direction. During the slow recovery stroke, the vorticity is weaker and is diffusing out in a rate more comparable to the its production, resulting in a weaker flow generation in the reversed direction.

In Figure 17, the time-averaged vorticity field for the different Re = 6 triangle input cases are shown, in which case (a) represents RH-1, case(b) is RH-2, Case(c) is RH-3, and case(d) is RH-4.

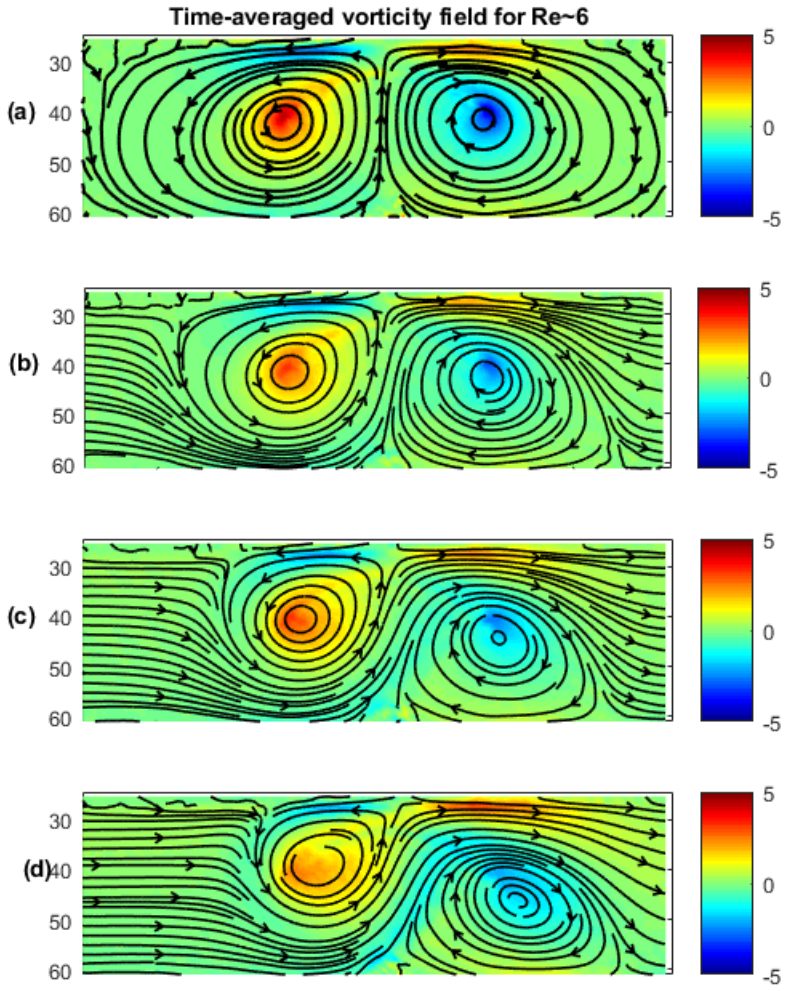

Figure 17.Time-averaged vorticity structures for Reynolds number=6 with triangle wave inputs a) RH1, b) RH2, c) RH3, d) RH4.

Asymmetry parameter increases in Figure 17 from ε = 0 to ε = 0.8 and clearly vorticity structure transform from two isolated fields in RH-1 to interconnected regions in RH-4. Vorticities become interconnected with higher strength as we increased the asymmetry parameter for RH cases. Flow is ejected from cavities between circulations in the pumping direction. In the case of ε = 0, two vorticities with the same strength mix the flow without any noticeable net pumping. More subtly, increasing asymmetry parameter shifts the symmetry of the strength and

spatial positioning of the vorticity distribution, enabling a net pumping. Specifically, the positive vorticity generated during the effective stroke is stronger. CW vortex forms during recovery stroke which has lower negative values. Former will shield the negative flow in the lower part of the channel in highly asymmetrical cases specially RH-3 and RH-4. Flow is being ejected from cavities between the swirling regions. Table 4 give the net pumping performance values are shown for RH and RL conditions. 3D effects are calculated by considering subtraction of inflow and its comparison to net pumping values of entire channel into the channel and it is reported in percentage.

Table 4.Pumping performance of different asymmetry parameters for different Reynolds numbers integration throughout the whole channel and corresponding 3D effects in the experiments

Asymmetry parameter (ε)	Π_t for Re = 6 (*10^-3)	Π_t for Re = 0.6 (*10^-3)	3D effects Re=6	3D effects Re=0.6
0	~0	~0	~0	~0
0.4	2.75	0.5	5%	4%
0.6	9.71	0.7	6%	3%
0.8	20	1.7	4%	4%

In the Table 4 , the pumping performance is calculated by integrating horizontal velocities in the x direction of entire channel. To calculate the 3D effects we evaluate at the horizontal velocity at the channel end (~1cm) and the beginning and compare it to the values from the entire channel. As is seen, the 3D effects are normally less than 5% with the maximum of no more than 7%.

Re number ~ 6 demonstrates higher pumping performances in comparison to Re number ~ 0.6. Less drag force from viscous medium and unsteady effects contribute to higher pumping performance in Re~6.

Non-reciprocal motion of a plate in presence of one-way flexibility

In the next segment of the study, the effect of an asymmetry in the stroke kinematics is examined by the introduction of a "one-way" hinge to the mid-chord of the plate. This is achieved by splitting the original plate into two equal length segments, and then joining back together with a thin, elastic tape, allowing the plate to be straight in effective stroke, but bend freely during the recovery stroke (see Figure 18). In addition to allowing for an asymmetric temporal kinematics as shown above, permitting the geometry of the gills to change during the effective and recovery stroke can accentuate the asymmetry and potential lead to increased effectiveness.

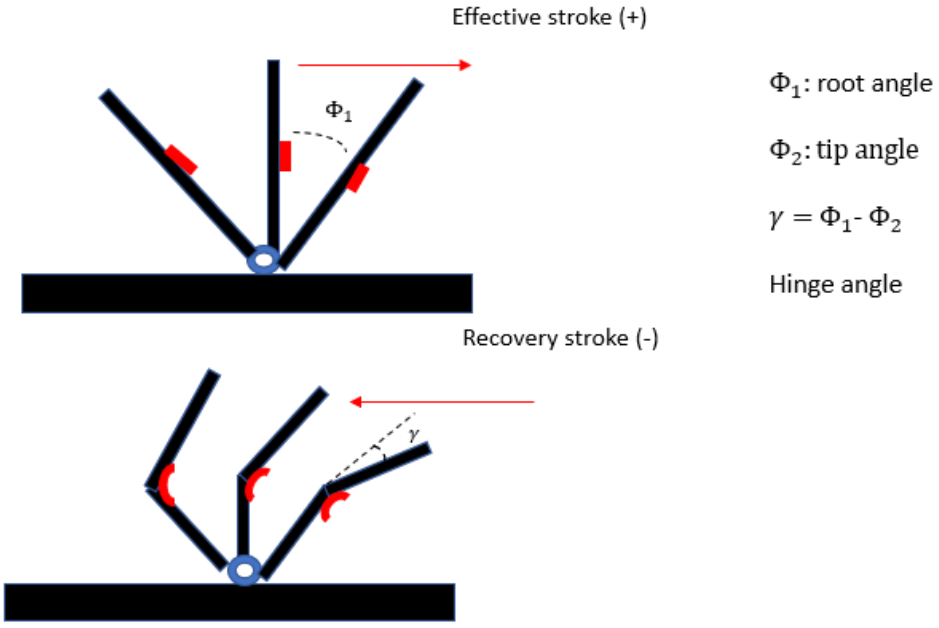

Figure 18. Root, tip, and the hinge angle in a plate in the presence of one-way elastic hinge.

For this case tracking of two points are required to obtain root angle (Φ_1) and the hinge angle ($\gamma = \Phi_2 - \Phi_1$). Two cases were studied with the flexible hinge, both of which had the same average Reynolds number of Re = $fl^2\Delta\Phi/\nu$ = 9, but with varying stroke angle and frequency to observe how changes in these parameters altered the net pumping performance. The first case had the nominally higher frequency (f = 0.88 Hz) but reduced stroke amplitude ($\Delta\Phi$ = 60°) and is hence referred to as the FF (flexible-fast) case. The second condition utilized a reduced stroke frequency (f = 0.5 Hz) and an increased stroke amplitude ($\Delta\Phi$ = 110°) and will be references as the FS (flexible-slow) case. The input waveform in both cases utilizes a sine wave, and the observed kinematics of both the root and tip plates extracted from the PIV images is for both cases is shown in Figure 19.

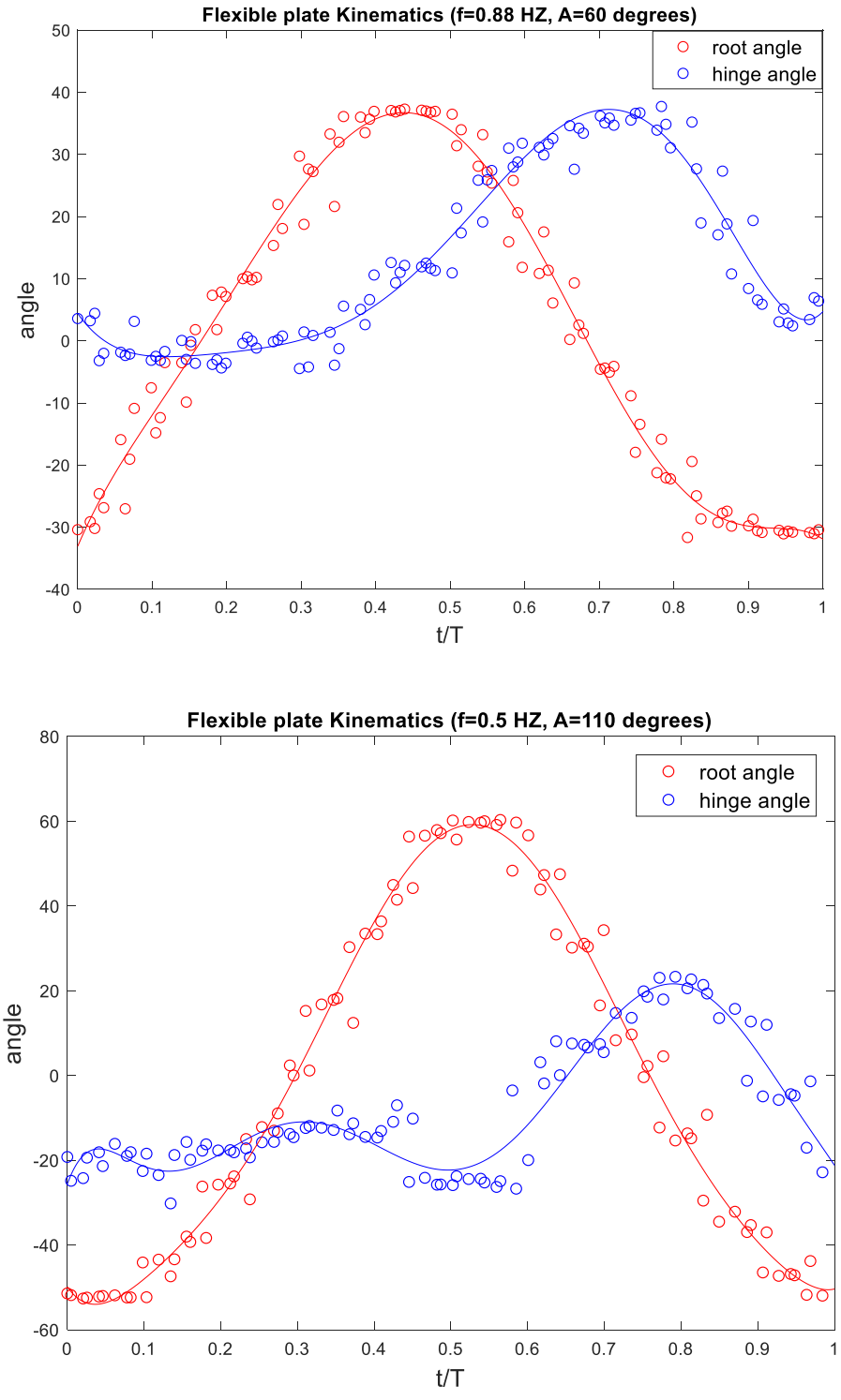

Figure 19.Root angle and hinge angle for two flexible cases with a) higher frequency (f=0.88 Hz) and lower amplitude (Amplitude=60 degree) b) Lower frequency (f=0.5 Hz) and Higher Amplitude (Amplitude=110 degree)

In the next Figure, instantaneous pumping performance is shown for FF and FS. In the Figure 19, FF is relatively straight during effective stroke but FS bends slightly backwards.

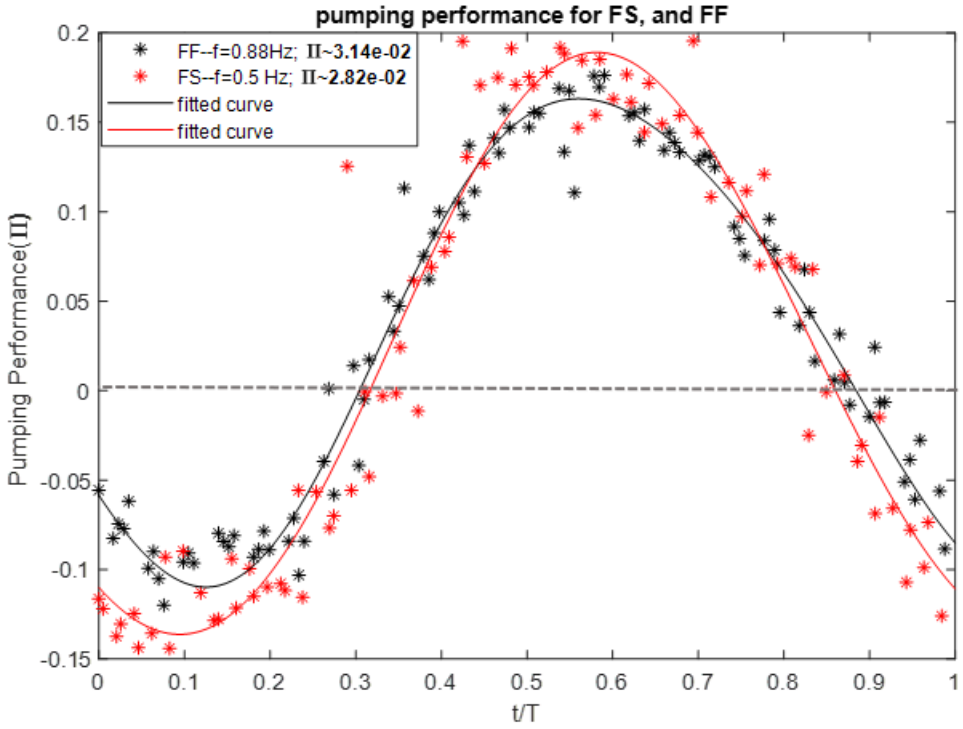

Figure 20.Pumping Performance for the flexible case a) frequency= 0.88 and Amplitude= 54 degrees b) frequency=0.5, Amplitude=120

The above is reflected in the phase-resolved pumping performance for the two different cases, as shown in Figure 20. Interestingly, the peak phase-resolved pumping performance is larger for the FS case, and the net pumping is seen to result in a greater net offset of the time varying curves.

Dissipation rate and efficiency

In the previous section pumping performance was introduced as a direct measure of the amount of fluid moved per unit time. From a biological as well as an engineering perspective, it is also important to know what energy is required to produce a given flow. From a general pump design perspecitve, this is typically represented by a non-dimensional efficiency that given by the net energy increase imparted to the pumped fluid divided by the energy consumed by the device at that given operating condition. For many applications that rely on species transport (such as respiration), this defination has been found to not be an effective measure of performance (Larson, *et al.*). They instead introduced the Mass-Specific Volume Flux (MSVF) as a more representative measure for conditions where overall mass transport, rather than energy imparted to the working fluid, is a functional priority. ($MSVF$) is calculated as the ratio the pumping performance (Π) to the time-averaged total work ($\bar{E}$), or $MSVF = \Pi/\bar{E}$).

To calculate the net work done by the oscillating plate, one would need to have the time varying viscous stress and pressure across the entire moving surface. Unfortunately, this is not possible with the current instrumentation. For the specific conditions of the current operating range and geometry, however, an approximate net measure can be provided by the time-averaged dissipation of the kinetic energy within a control volume surrounding the local oscillaitng plate region. This leap is predicated on the assumption that no significant net kinetic energy is convected out of the control volume of observation, hence there is an approximate balance between the work input and dissipation. A more lengthy development of this argument, and

justification within the current work, is given in Appendix A. This assumption has also been used and verified through comparison to DNS simulations at slightly higher Reynolds numbers in a three-dimensional flow generated by a robotic oscillating plate array in the work of (M. Larson et al. 2014), where it was found that the time-averaged dissipation within the control volume approximately one plate length surrounding the array was equal to the time-averaged work done by the plates to within 2%.

This estimate of the work done by the oscillating plate will be used to provide a measure, albiet imperfect, of the pumping efficiency for the different cases. The phase-resolved dissipation within the control volume will also be discussed to better understand the portions of the cycle and hydrodynamic behaviors that are associated with the peak energy consumption, but it will not be used to discuss a phase-resolved MSVF, as the approximate equality between the work and dissipation has only been more strongly established in a time-averaged sense.

Dissipation is the energy loss due to irreversible viscous shear work of the fluid and it is calculated as follows for a 2D flow:

$$\gamma = \mu\left[2\left(\frac{\partial u}{\partial x}\right)^2 + 2\left(\frac{\partial v}{\partial y}\right)^2 + \left(\frac{\partial u}{\partial y} + \frac{\partial v}{\partial x}\right)^2\right] \quad (18)$$

All the input energy from a gill dissipated within a short distance from generation site due to the relatively small Reynolds number. The average of energy dissipated within a control volume is calculated as:

$$\bar{E} = \frac{1}{T}\int_0^T \int_0^H \int_0^L \gamma(x.y.t)dxdydt \quad (19)$$

In which “L”, and “H” represent the length and the height of the imaged region around the gill. $\bar{E}$ has to be non-dimensionlized for a comparison between different cases. The stroke amplitude, $\Delta\Phi$, frequency, f, and gill length (l_g) are used to non-dimensionalize $\bar{E}$, resulting in a grouping $\rho f^3 L_g^4 \Delta\Phi^2$.

Table 5. Different wave forms with different pumping performance and MSVF

CASE	Asymmetry parameter (ε)	Π_t for Re = 6 (x10^{-3})	Total work (x10^{-3})	MSVF
RH1, Triangle—Rigid plates	0	~0	6.8	0
RH2, Triangle—Rigid plates	0.412	2.7	5.4	0.5
RH3, Triangle—Rigid plates	0.64	9.7	5.6	1.73
RH4, Triangle—Rigid plates	0.84	20	8.3	2.4
FS, Sine (ΔΦ=96°, f=0.5 HZ)	NA	28	10	2.8
FF, Sine (ΔΦ=54°, f=0.88 HZ)	NA	30	9.7	3.09

Table 5 lists the experiments for a Reynolds number of approximately 6 presented in this thesis. The Re = 0.6 conditions were omitted, as the noise levels from the velocity interrogations were high enough to render the velocity gradients estimates to be questionable for estimation of the dissipation.

Examining the results in Table 5 , it can be seen that the FF case provided the greatest overall efficiency of the group (MSVF ~ 3.1), edging out the FS condition by approximately 10%, and exceeding the best rigid plate case by 30%. The dissipation of the FF and FS cases are largely comparable, indicating the greater efficiency is largely due to the increased pumping performance. In examining the rigid plate cases, MSVF is smaller than the flexible conditions, and also grows monotonically with the

asymmetry parameter. This is indicative of the possibly increased resistance and dissipation incurred by the rigid plate during the recovery stroke, and will be examined in greater detail below.

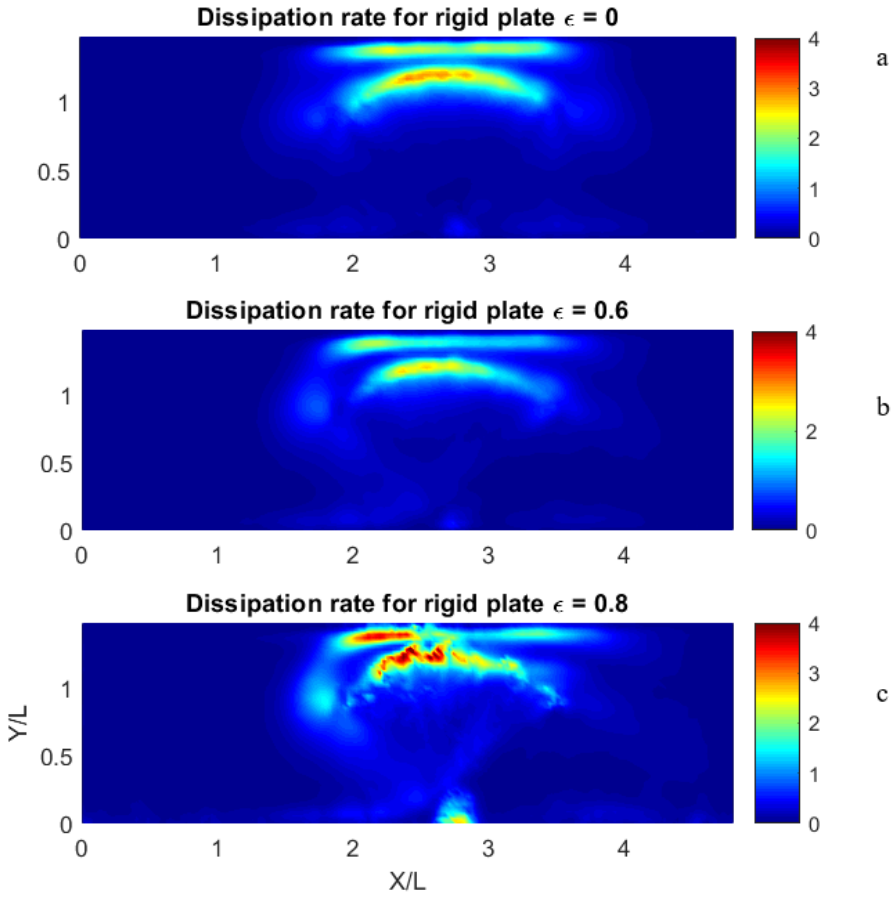

Figure 21. Dissipation rate for a) symmetric case, a) RH-1 b) RH-3 c) RH-4

The spatial distribution of the time-averaged dissipation is shown in Figure 21. Case RH-1 is shown in Figure 21.a, corresponding to the symmetric motion in which the rigid plate ocsillate back and forth at a constant speed, producing a flows that will mix without finite pumping. Figure 21.b ,RH-3, shows a distinct asymmetry in the average dissipation, consistent with the stronger vorticity production and rapid

disspation that occurs during the rapid motion of the effective stroke, producing a MSVF ~ 1.73. Case (c) corresponds to condition RH-4, which demonstrates a similar, but more exaggerated asymmetry peaking near the wall where more shearing occurs. Note that the irregular shape of the dissipation in this plot is due to the very short duty cycle of the effective stroke, resulting in a finite number of distinct positions to be included in the time-averaged ensemble. Interestingly, despite having a nearly 50% increase in the total dissipation as one move from case RH-3 to RH-4, the overall efficiency is highest for the RH-4 condition. This results from the greater relative increase in the net pumping (approximately 100%) over that of the dissipation. Examining the flexible cases FF and FS (Figure 22), demonstrates that the dissipation is also slightly asymmetric as a result of the flexure during recovery stroke. The FS case is spread laterally to a greater extent, consistent with the greater stroke amplitude, while the magnitudes are generally larger for the FF case.

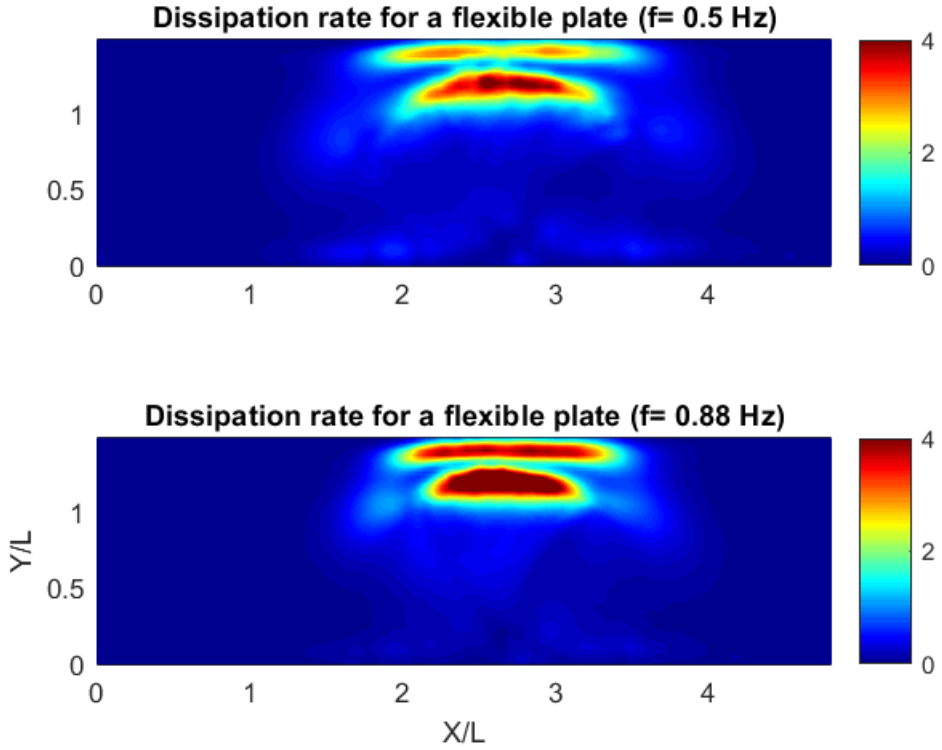

Figure 22.Dissipation rate for two different flexible cases with the same Reynolds number but different input amplitude and frequencies (a) case FS, (b) case FF.

In a net sense, these differences largely compensate one another, resulting in an average normalized dissipation that is only 3% for FS case in comaprison to the FF condition. Thus we see that for a fixed Reynolds number condition, increased frequency of the actuation with a smaller amplitude for a flexible gill results in both a higher pump rate and a slightly reduces dissipation. It would be interesting for future work to examine a wider range of amplitude and frequency conditions to see if and where an optimal condition may be found for a given Re. One may expect this to be tied, perhaps, to the formation and shedding of the vorticity in the flow, and the time scale required for the passive flexure to respond to the flow variations within the cycle.

Figure 23 demonstrates instantaneous dissipation rate in a cycle for two flexible cases at a same Reynolds number (FF and FS).

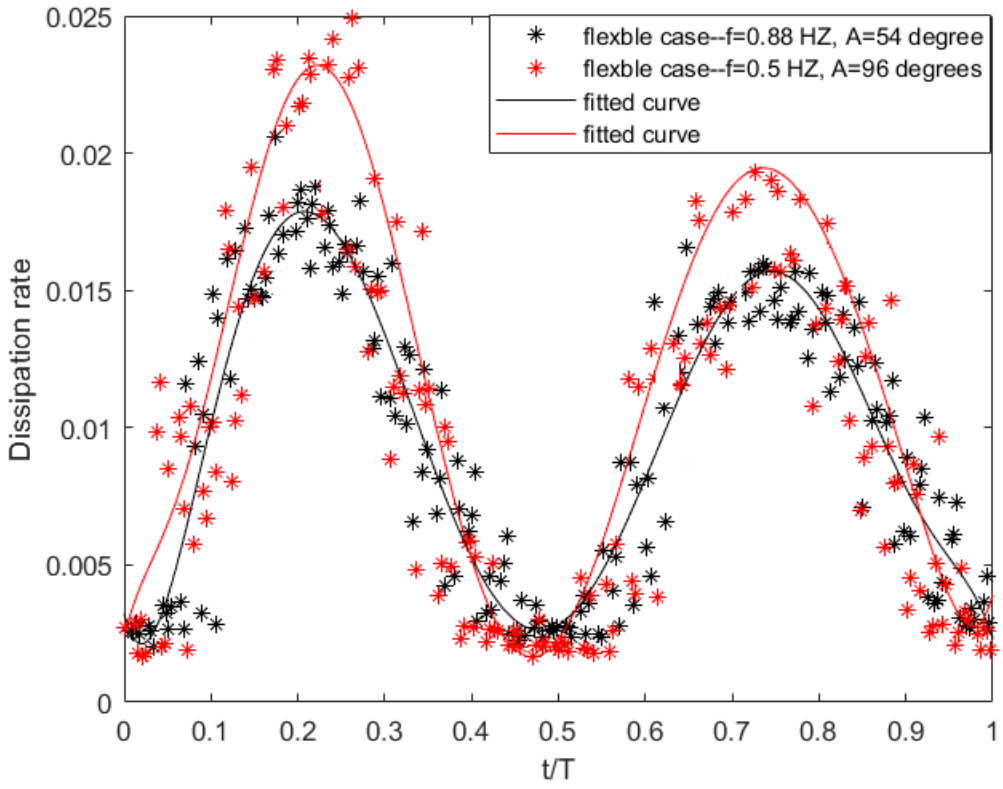

Figure 23.Dissipation rate for two different flexible cases with the same Reynolds number but different input amplitude and frequencies (a) case FF, (b) case FS.

Two peaks are seen in Figure 23 which correspond to time when the plate tip is passing closest to the opposite wall, first during the effective stroke (t/T = 0.25) and the secound during the recovery stroke (t/T = 0.75). During the recovery stroke plate flexes which will increase the gap between the channel's upper wall and the plate's tip. This will relatively reduce the dissipation rate which is reflected in Figure 23(a) and (b).

In Figure 24, the phase-averaged dissipation ratse for cases RH-1 though RH-4 is shown. RH-1 and RH-2 (Figure 24a) demonstrate lower instantaneous dissipation values in comparison to RH-3 and RH-4 (Figure 24b). RH-1 indicates two equally-spaced sharp peaks, followe by a gradual decay. These correspond to the time shortly after stroke reversal, with similar dissipation magnitudes for both effective and recovery stroke. For the RH-2 case, a second peak is also visible at just after transition to recovery stroke, which reached 70% of the first peaks value at a non-dimensional time of $t/T = 0.5$. This lowered value is due to lowered plate's speed in the recovery stroke.

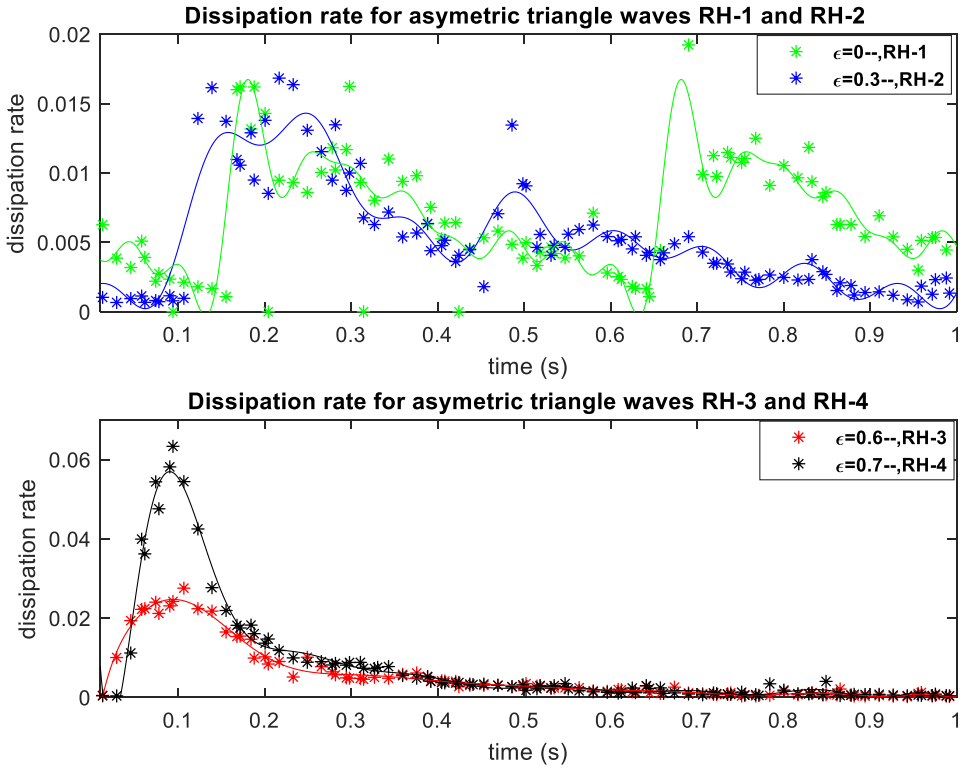

Figure 24.Dissipation rate for four triangle actuations a)RH-1, RH-2 b) RH-3, RH-4

In Figure 24 b, the increased temporal stroke asymmetry results in a dramatic increase in the dissipation values of the first peak, and a disappearance of any perceptible second peak. The maximum dissipation for the $\varepsilon = 0.8$ is observed to be more than twice the peak values for $\varepsilon = 0.6$. The dissipation during recovery is not appreciably different between the RH-3 and RH-4 cases, resulting in a higher average dissipation for the greater asymmetry cases.

To sum up this chapter we ephasize on some key points. Asymetrcal triangle waves were studied and Among all the cases, $\varepsilon = 0.8$ demonstrate the highest MSVF and pumping performance. total work is the highest for $\varepsilon = 0.8$, but noticeable pumping performance will compensate and therefore MSVF is increased. As asymmetry parameter decreases these values also plummet. Instantaneous dissipation rate

indicates two peak values for a flexible case in which first peak has higher values. The plate is straight in the effective stroke with more contribution to the dissipation rate. It bends during the recovery stroke and will result in decreasing momentum transfer from a plate and lowered dissipation rate. Straight plate in effective stroke will get closer to the wall where shear work is higher, and this corresponds to the first peak. Bent plate is further from the wall and will cause less dissipation. MSVF is 10% higher for FF due to higher pumping performance and lowered total work. In the case of symmetrical triangle waves, dissipation rate indicates two similar peaks with same amplitude. As asymmetry is introduced second peak start to decrease and it is vanished in the cases of the highest asymmetry (RH-3 and RH-4).

Chapter 4: Pumping of array of five plates in a channel

After single plate experiments which is widely seen in nature in species like scallop and jellyfish, more plates are added to experiment pumping in an array of five plates. It is seen in the nature that array of multiple plates and their inter-gill hydrodynamic interaction can noticeably enhance pumping in different organisms such as Mayfly. The parameters for the study include: 1) inter-plate phase difference, 2) asymmetry of the protraction/retraction stroke speeds, and 3) the presence of a one-way elastic hinge. Synchronous motion of rigid plates with symmetrical/harmonic input actuation signals (e.g. Sine waves) generates zero pumping. Questions to be answered in this chapter are:

1. How one-way flexibility will enhance pumping, and the pumping efficiency in the array of five plates?
2. How utilizing combination of inter-plate phase delay ($\Delta\theta_i$=90) and one-way flexibility will enhance pumping and MSVF beyond the use of either individually?
3. does antiplectic, and symplectic wave propagation improve the pumping performance and pumping efficiency in the asymmetrical triangle wave inputs?

Problem definition:

We carried out the experiments in a channel of length L, height H, containing equally spaced plates that are arranged perpendicular to the channel. A generalized wave input wave form $f(x.t)$ which varies in space and time could be used for actuation and each plate could be controlled individually. $\Delta\theta_i$ is the phase lag between adjacent

plates and will provide different metachronal motions in the array of five. In the first two experiments, sine wave actuation is used in an array of five plates.

After two preliminary experiments, asymmetrical triangle wave input is implemented to provide for a faster effective stroke than recovery stroke (~2.5 times faster). Metachronal motion is applied to both sine wave actuation and asymmetrical triangle actuations.

Basic metachronal motion is illustrated in Figure 25, where two different metachronal motions are illustrated using a harmonic rotation of the plate about its root location. Figure 25a demonstrates synchronous motion with $\Delta\theta_i = 0$. Figure 25b shows a phase lag of one quarter cycle ($\Delta\theta_i = 90$) between adjacent plates. Assuming the fluid is pumped in the net positive direction, the latter condition is referred to as antiplectic metachroal motion, as the travelling wave (moving to the left) and the net pumping direction (moving to the right) are in opposition to each other.

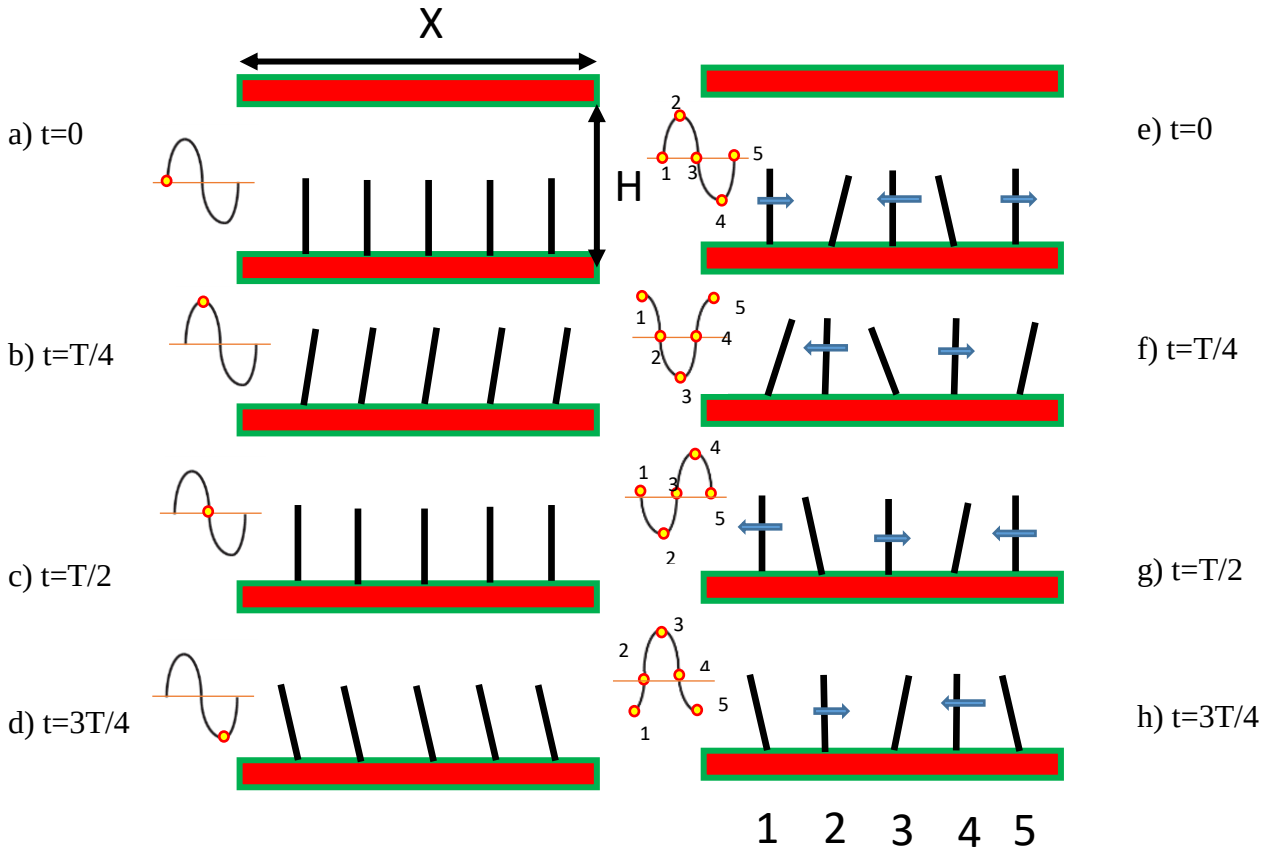

Figure 25. Schematic picture of the problem. 1) plates beat in phase 2) plates beat out of phase ($\Delta\theta_i = 90$). First plate is in a) the middle of effective stroke at θ=0. b) At the end of effective stroke θ=φ⁄2. c) middle of recovery stroke θ=0 .d) end of recovery θ=-φ⁄2

In the Figure 26 case (1), 5 gills are in synchrony and they beat in phase. In (2), however, there is a 90 degrees phase lag between them. Blue arrows in (2) demonstrate the direction of plates in 90 degrees phase lag metachronal motion. Kinematics and directionality of plates in (2) will be used later in the paper to explain Kinematics of hinged plates and flow field in the channel.

Figure 26 demonstrate schematic of five oscillating plates in the channel. Plates are Attached to the acrylic rod in which the shaft is placed in the groove and it can oscillate freely.

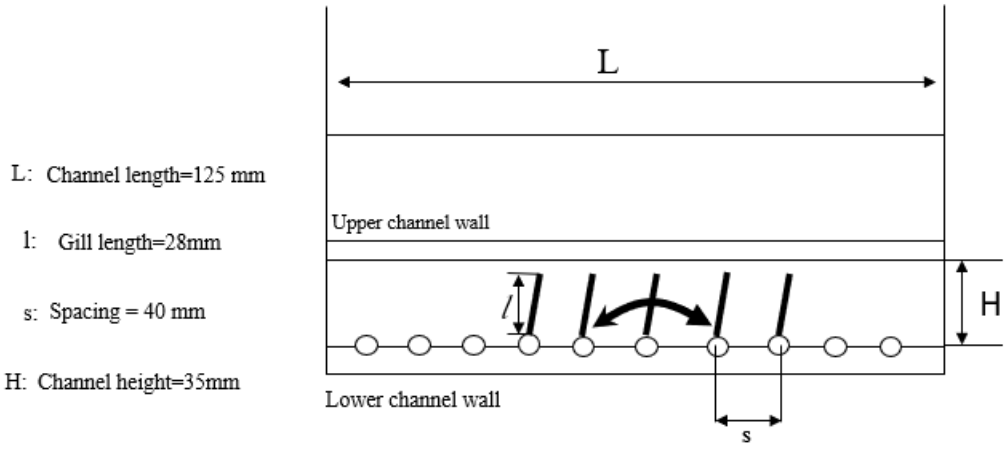

Figure 26. Schematic and dimension of five plates in the channel.

Results

Test condition

To elucidate the effect of close interaction of the plates, a series of experiments replicating the kinematics of the single plate tests were designed and conducted. Although a much wider series of tests were conducted, which is tabulated in the appendix b. In the post analysis, two flexible plate tests and four rigid plate tests were of appropriate quality for confident analysis and are summarized in Table 6.

Table 6. Different experimental conditions in an array of 5 oscillating plates

Case name	$\Delta\theta_i$	ϵ	**Plate type**	**Frequency (HZ) Amplitude (°)**	**Wave form**	**Pumping performance**
SR0	0°	NA	Rigid	0.6 /72	Sine wave--Synchronous	0.0
SF0	0°	NA	Flexible	0.6 /72	Sine wave--Synchronous	0.05
SAF90	-90°	NA	Flexible	0.6 /72	Sine wave--Antiplectic	0.13
TR0	0°	0.6	Rigid	0.4/72	Triangle--Synchronous	0.03
TAR15	-15°	0.6	Rigid	0.4/72	Triangle--Antiplectic	0.05
TAR30	-30°	0.6	Rigid	0.4/72	Triangle--Antiplectic	0.03
TsR15	+15°	0.6	Rigid	0.4/72	Triangle--Symplectic	0.07
TsR30	+30°	0.6	Rigid	0.4/72	Triangle--Symplectic	0.12

In the case names: “S” stands for the sine wave actuations and “T” is asymmetrical triangle wave with $\varepsilon = 0.6$. “A” is antiplectic wave and “s” is symplectic. “R” is the rigid case and “F” is in the presence of flexibility. The number at the end is $\Delta\theta_i$ which is the phase lag between flexible plates.

In the first two experiments, a symmetric sine wave input signal is used to actuate flexible plates. Plates are relatively straight in the effective stroke, but they bend in the recovery stroke. Pumping performance is 0.05 when plate beat in synchrony as

seen in the Table 6. When a -90° antiplectic phase lag is introduced between adjacent plates, the pumping performance is observed to noticeably increase. In the result section, details of the flow structure will be reviewed to explain the reasoning behind increased pumping performance with the introduction of the metachronal motion.

In the next sets of experiments, an asymmetric triangle input wave is used for the actuation of the array of five rigid plates. The asymmetry parameter is set to a constant value of $\epsilon = 0.6$ as a representative case, selected from the wide range of conditions that could be implemented in conjunction with metachronal motion. This condition is then examined for three different phase delays ($\Delta\theta_i$ = 0°, 15°, 30°) are implemented to study the effect of increased inter-plate phasing on the pumping performance. Metachronal phase delay could be implemented in two different fashions so-called symplectic or antiplectic, which corresponds to a change in the propagation direction of the travelling wave. Symplectic metachrony is when the input metachronal actuation is moving in the same direction of net pumping. In antiplectic actuation, however, as explained before, metachronal actuation and pumping direction are in the opposite directions.

In reviewing the summary information in Table 6, case SAF90 utilizing an antiplectic metachronal sine wave actuation of 5 flexible gills with phase lag -90◦ provides the highest overall pumping performance ($\Pi = 0.13$). This is followed by symplectic sawtooth wave actuation of 5 rigid gills with 30◦ phase lag between adjacent plates ($\Pi = 0.12$). A phase lag of 15◦ represents a relatively small difference in the motion between adjacent plates, which results in minimal hydrodynamic interactions between the plates. As indicated, a small phase differences seems to be a more effective pumping strategy for antiplectic metachrony rather than symplectic motions. Symplectic metachrony, however, provides a higher pumping performance for larger of the two phase delays tested (30° and 15°, respectively). Later in the thesis, it will be shown that the energy dissipation rate is noticeably lower for the small phase differences between plates.

Synchronous motion of five rigid plates

Experiments are carried out with 5 plates and detailed inter-appendage interaction between adjacent plates are captured in PIV images. The first test conducted utilizes a temporally symmetric waveform (sine wave) applied to a rigid plate with no phase delay (synchronous motion). This represents a baseline case which is the simplest possible extension of the rigid single gill test case. Again, no net pumping is expected, but the interactions that are produced can provide a useful baseline comparison.

The frequency of oscillation was specified as 0.6 Hz, and the amplitude was 72 degrees giving a Reynolds number of approximately 6. Recovery and effective strokes actuation kinematics are identical for this case and the flow oscillates in a symmetrical fashion for $\Delta\theta_i = 0$. Figure 27 represents 4 ensemble-averaged velocity contours at specific phases in the cycle, and the fifth image is time-averaged velocity field of all 500 PIV images. The plates shown in Figure 27a are stationary at the end of recovery stroke transitioning to effective stroke at $(\Phi = 0, t = 0)$ with velocity magnitudes to the left. Figure 27b is captured at the middle of effective stroke, $t/T = 1/4$,where the plates are at their maximum speed to the right. In the Figure 27d plates are stationary and transitioning to a recovery stroke. they are at the same location as Figure 27b but are at peak velocity during the recovery stroke. Figure 27d depicts the end of recovery stroke where stationary plates are again stationary and transitioning to the start the effective stroke.

Plates are rigid and their reciprocal motion result in zero pumping performance since effective stroke is identical to recovery stroke. In Figure 27, the flow in case(a) is

counterbalanced by case(c), and the pumping direction in case (b) and (d) are in symmetric opposition. The time-average shown in case (e) is characterized by isolated vortices with zero pumping performance.

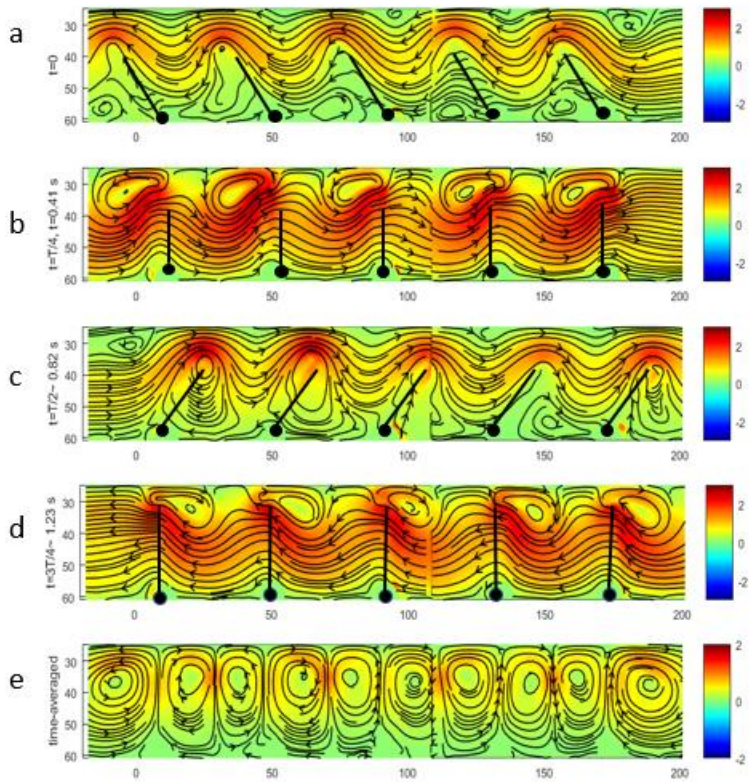

Figure 27. Ensemble-averaged non- dimentionalized velocity magnitude fields for SR0. a) ensemble-averaged velocity field at t=0 . b) ensemble-averaged velocity field at t=T/4 c) ensemble-averaged velocity field at t=T/2 . d) ensemble-averaged velocity field at t=3T/4 e) Time-averaged case.

Asymmetric input actuation and metachronal waves

Sine wave actuation of five flexible plates

In the first experiment, 5 rigid plates are oscillating back and forth in a symmetrical fashion utilizing a sine wave actuation. For rigid plates in synchrony, a symmetric actuation is expected to produce zero net pumping due to identical effective and recovery strokes, (Figure 27e) which is indeed borne out by the calculated pumping performance for this case.

One-way flexibility is introduced to the rigid plates and will result in a non-reciprocal motion that is expected to produce a net finite pumping. In the non-reciprocal input motion, each plate generates pair of vortices but, asymmetry in flexible plate's non-reciprocal motion will result in displacement of vortices which make them interconnected. This can be verified in Figure 28e.

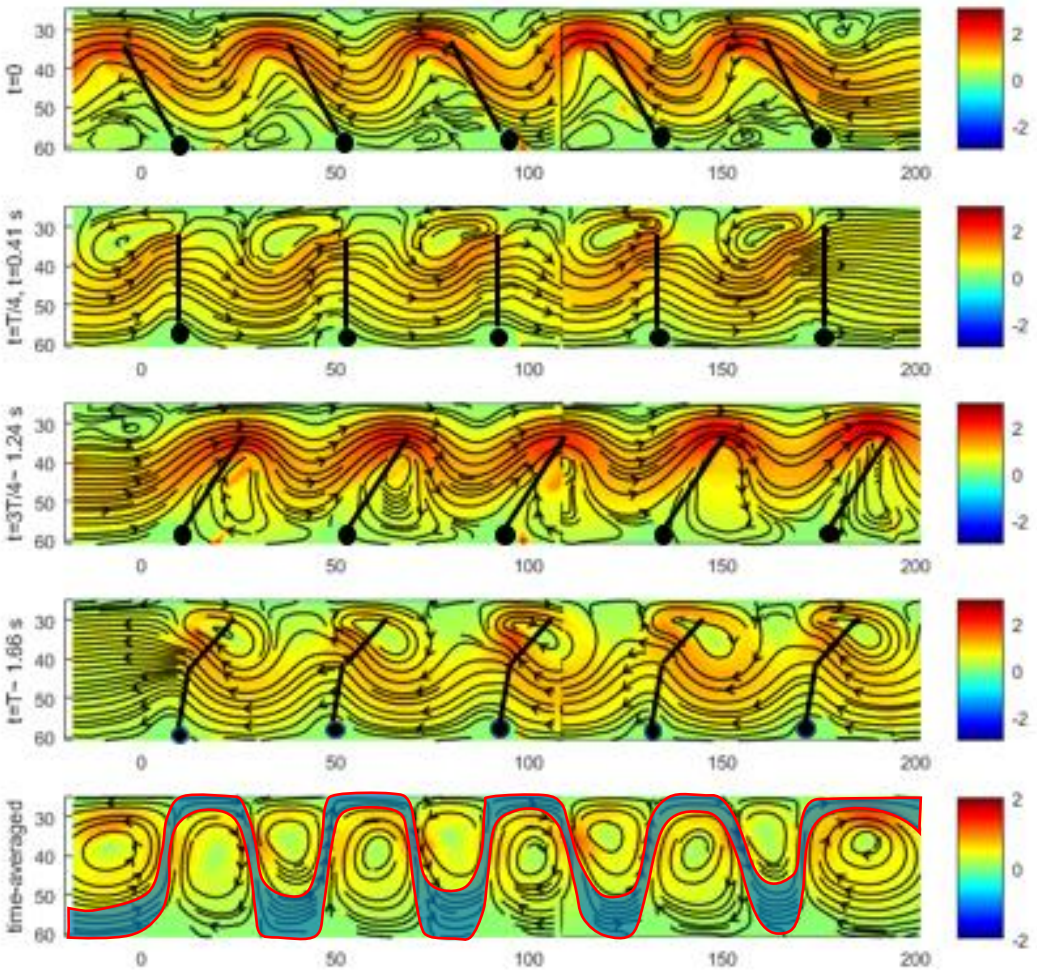

Figure 28.Ensemble-averaged velocity fields for five flexible plates SF0. a) ensemble-averaged velocity field at t=0 . b) ensemble-averaged velocity field at t=T/4 c) ensemble-averaged velocity field at t=T/2 . d) ensemble-averaged velocity field at $t = 3\frac{T}{4}$ e) Time-averaged case, connected streamline in the pumping direction from left to right.

Figure 28 demonstrates synchronous oscillating sine motion of five hinged plates. The plates are straight during the synchronized effective stroke, as shown in figures 28a and 28b , which results in a strong streaming motion throughout the array, which can be seen in the Figure 28e. The elastic hinge flexes noticeably during recovery

stroke, producing a reduced effective area of the plate results in a decreased flow in that direction (Figure 28d). Averaging all the velocity fields over time at different phases in a cycle will result in a time-averaged field, which consists of series of interconnected roll cells that are weakly connected by a meandering streamtube at their periphery, resulting in a small but noticeable net pumping from left to right ($\Pi = 0.05$).

To further improve the pumping observed in the synchronous case with one-way flexibility, a phase delay of -90° applied between adjacent plates. To document the actual kinematics executed by the feedback control system, the motion of each plate has been extracted by tracking the root and distal plate tip from the PIV images at 10 different phases throughout the cycle. In Figure 29, the history of the root and hinge angle observed are recorded. The -90° phase delay between adjacent is clearly visible and reproduces the intended motion with reasonable fidelity. There is a greater variability in the hinge angle behavior, due to the small differences in the construction of the plate assemblies, as well as the variable hydrodynamic loading on the distal plate.

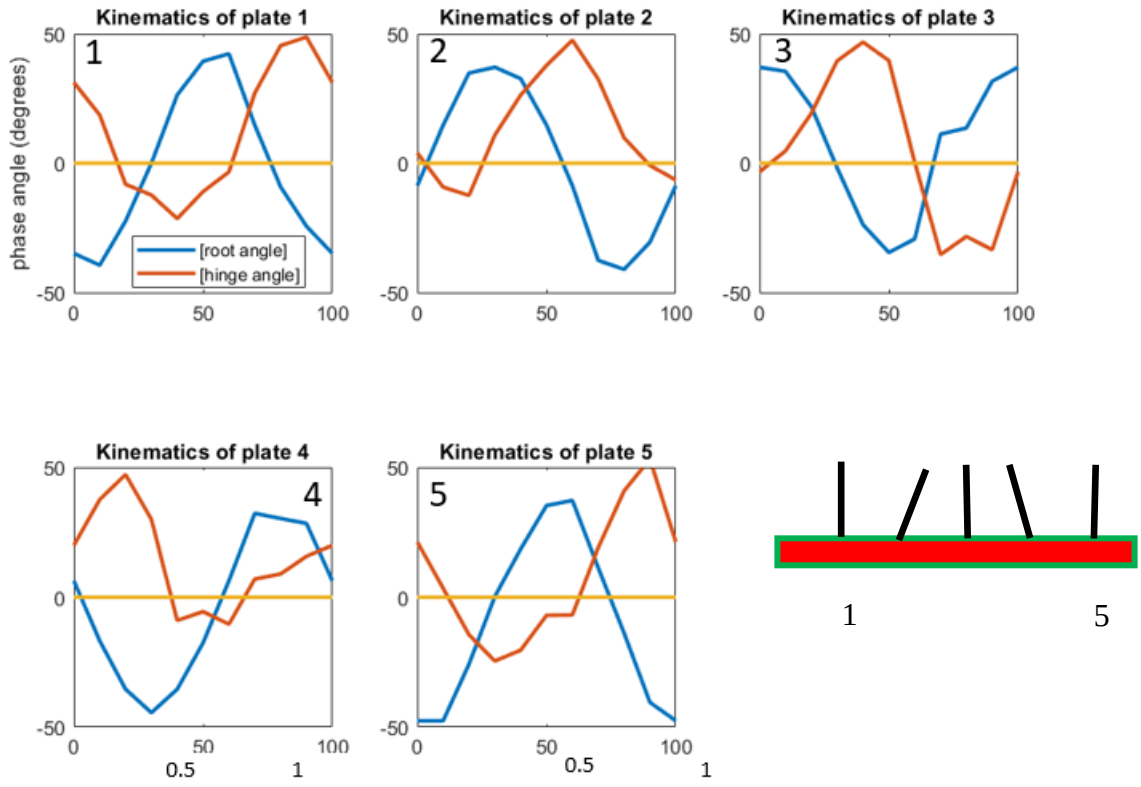

Figure 29. Observed kinematics of flexible plates in an array of 5 flexible plates for case SAF90, reporting the root and hinge angle.

Ideally, the distal plate would have a minimal deflection to the negative hinge angle direction during the effective stroke, and a major positive deflection during the recovery stroke. Although the hinge angle deflection is noticeably biased toward the positive direction, some of the plates show up to a 30° prolapse during the effective stroke (see plate 3, for example). Multiple attempts were made to refine the plate construction to minimize this behavior, and the reported results represent the best results obtained. The hydrodynamic effect that also contributes to this can be observed in the details of Figure 30, at t/T = 0.75 where plate 3 is in its peak effective stroke and trying to generate a flow counter to plates 1 and 5, which are both 180° out of phase with plate 3, and in their peak recovery stroke (see Figure 30 d).

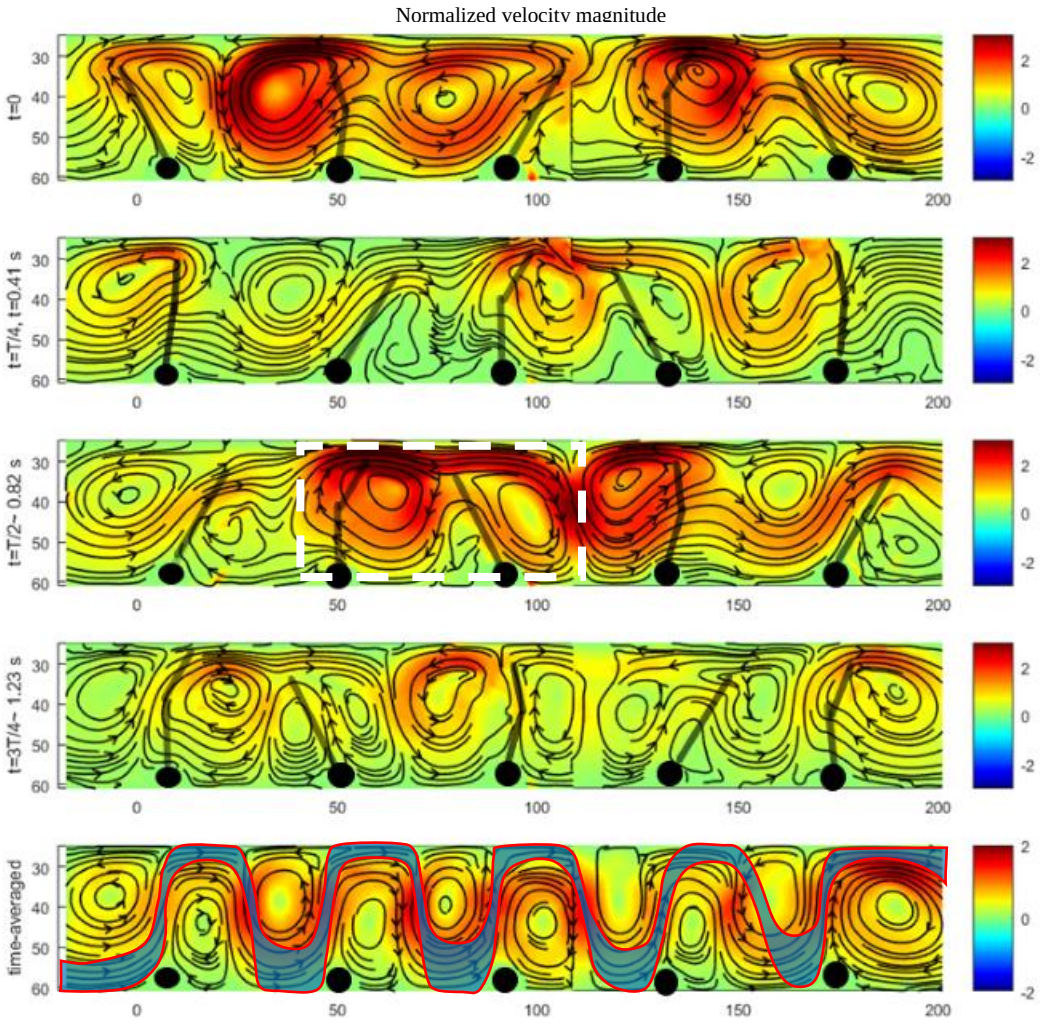

Figure 30. Ensemble-averaged normalized velocity magnitude fields for SAF90 a) ensemble-averaged velocity field at t=0. b) ensemble-averaged velocity field at t=T/4. c) ensemble-averaged velocity field at t=T/2. d) ensemble-averaged velocity field at t=3 T/4 e) Time-averaged case. F) connected streamline in the pumping direction from left to right. White box points out the region of shielding effect.

We previously emphasized on the advantage provided by plate flexibility in the recovery stroke. One-way flexibility becomes even more effective in conjunction with antipletic metachrony with $\Delta\theta_i = -90°$, where the pumping performance is improved by a factor of approximately 260% from Π =0.05 to 0.13. Figure 30 c at

t/T = 0.5 depicts the conditions of the greatest instantaneous pumping due to effective hydrodynamics interactions. The instantaneous pumping performance shown in Figure 31 verifies the qualitative impressions given by Figure 30c. The white dashed box shown in Figure 30c at $t/T = 1/2$ will single out a phenomenon (shielding effect) in which it will result in a higher pumping performance for this case (S.N.Khaderi et al. 2009). At this phase, plate 1 is at the end of the effective stroke with a positive net pumping to the right. Plate 2 is in the middle of recovery stroke with smaller negative flow because of less resistance due to the bending of the elastic hinge. A clockwise recirculation cell is formed on plate #2 and #3 which will shield their negative flow from the positive stream. This will direct the positive flow from plate 1, along the top wall where it is eventually merged with positive flow being produced by plates 4 and 5 at the exit of the channel. The clockwise recirculation cells are helpful to the pumping performance for this case, as the induced velocity of the vorticity is positioned to assist in the positive current on the top wall. This phenomena was observed by (Khaderi, Den Toonder, and Onck 2011) in their work in low Reynolds number, and referred to as a "shielding effect".

In the Figure 30b, plate 1 passes $\Phi = 0°$. at $t/T = 0.25$ with a maximum velocity in the positive direction. Plate 2 is straight at the end of its effective stroke and has finished its contribution to the positive flow. Plate 3 and 4 are in recovery stroke generating the clockwise circulation cell in which the negative flow is again shielded from the positive stream. Figure 30e shows the time-averaged streamlines and velocity magnitude of combined 500 PIV images. The mean flow is qualitatively similar to that for flexible plates moving in a synchronous fashion, with the exception

that it has a stronger meandering band of positive net flow moving fluid from left to right ($\Pi = 0.13$). The clockwise circulation cells formed within the array occur at the beneficial time to assist in producing an increase in the net flowrate.

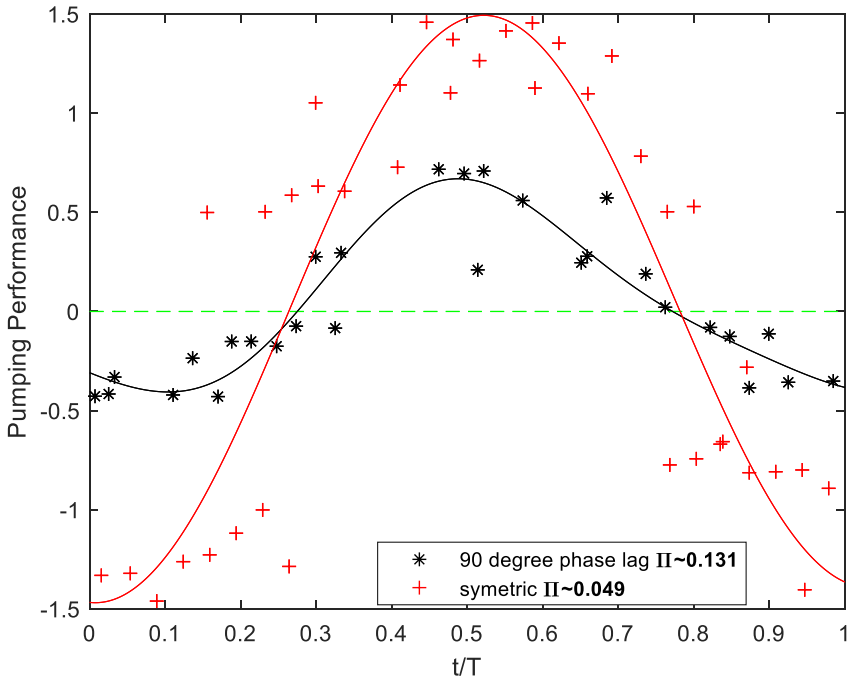

Figure 31.Instantaneous pumping performance for 5 flexible plates. a) SF0 (red markers) b) SAF90 (black markers).

Asymmetric triangle actuation of 5 plates

After sine wave actuation of 5 flexible appendages in the last chapter we study the effect of triangle wave input on pumping. In the first case TR0, 5 rigid case oscillate back and forth in the presence of triangle wave with the asymmetry parameter of $\varepsilon = 0.6$. In the next two cases TAR15 and TAR30, antiplectic wave propagation is studied in which metachronal wave travels in the opposite direction of pumping. In the last two cases TsR15, and TsR30 metachronal wave and pumping are in the same direction. We hope to answer the following questions:

1. Is antiplectic or symplectic wave propagation is more effective strategy for pumping in triangulate actuations of rigid plates?
2. Which of former strategies are more efficient with the higher MSVF?
3. How does increasing phase lag would alter the pumping curve in antiplectic and symplectic wave propagations and why?

Figure 32 demonstrate the instantaneous pumping performance for the antiplectic metachronal motion using triangle wave kinematics ($\varepsilon = 0.6$) for the array of five rigid plates.

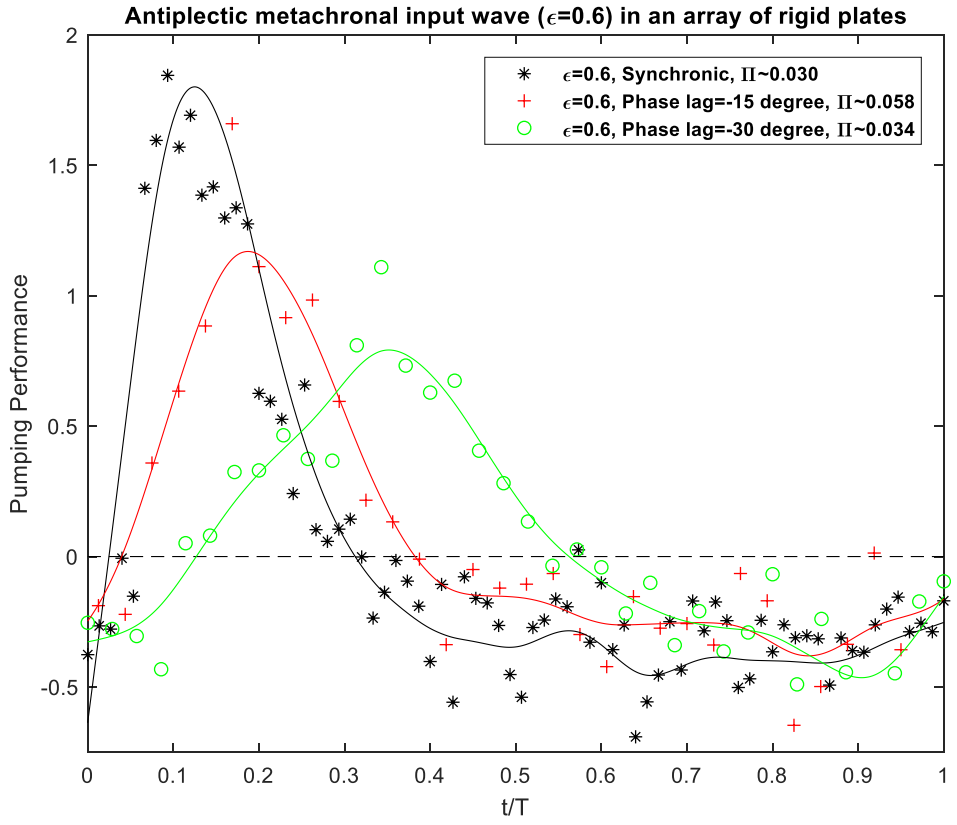

Figure 32.Instantaneous pumping performance for 5 flexible plates. A) TR0 (black markers) B) TAR15 (red markers) C)TAR30 (green markers)

In the Figure 32, three different instantaneous antiplectic metachronal motions are displayed. The black markers represent 5 rigid plates in synchronous motion using the asymmetric triangle waveform with $\varepsilon = 0.6$. The highest instantaneous net pumping is reached in this case because the whole array contributes to the pumping during the effective stroke. The duration of the effective pumping, however, is smaller than cases with metachronal actuations.

For the TAR15, $\Delta\theta_i$ = -15°, and represents a relatively small phase difference between the plates that results in the highest pumping performance among three cases. One can also view the phase delay as a wavelength of the travelling wave that

has a wavelength of $\lambda = 2\pi l/\Delta\phi$, where l is the spacing between the actuator plates in the array. Smaller phase delays then correspond to longer wavelengths, with neighboring actuators being closely aligned in their position. As a result, for a finite length array, a larger phase delay will result in a longer effective pumping duration, but maximum pumping performance is decreased due to the increased possibility of counter-oscillating plates degrading the overall performance. A smaller pumping performance occurs for the higher $\Delta\theta_i$ is because of returning plates in the recovery stroke causing a decreased maximum instantaneous net pumping. There is a tradeoff between increased effective pumping duration and the decreased maximum pumping performance. For the relatively small number of cases tested, the higher pumping performance occurs at around $\Delta\theta_i$ =15 for the antiplectic input wave for the rigid five plates and $\varepsilon = 0.6$. Figure 33 depicts the instantaneous pumping performance for symplectic metachronal motion of five plates. With a reversal of the wave propagation direction, the trend in pumping performance is now achieved for larger of the two phase delays ($\Delta\theta_i$ = +30°).

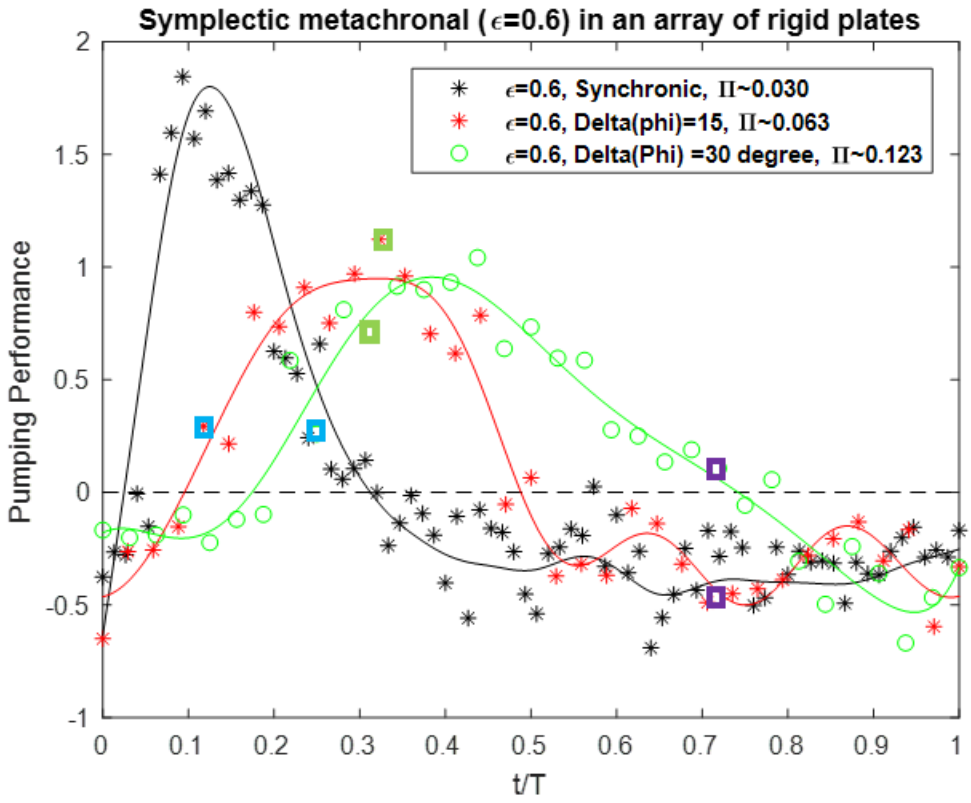

Figure 33.Instantaneous pumping performance for triangle/symplectic actuation of 5 rigid plates a) TR0, b)TsR15, c)TsR30

For these conditions, the pumping performance curves demonstrate a more gradual increase and decay of instantaneous pumping (Figure 33), which is in contrast to the trends of antiplectic case shown previously (Figure 32). The highest pumping performance occurs for greater phase lag $\Delta\theta_i$ = +30°, which can be related to a longer effective pumping period and will be explained in Figures 34, 35and 36 by looking at detailed flow structure at specific phase.

To explain the details behind the pumping curves observed in Figure 33, six different instantaneous velocity fields are selected at specific phases throughout the cycle for comparison. The first phase is where each condition first produces a positive net flow

(marked by the blue marker in Figure 33, and is shown in Figure 34). It is followed by peak values in the pumping performance (shown by the green marker box, shown in Figure 35) and then followed by a comparison of the phase where $\Delta\theta_i$ = +30° case finishes the effective pumping to explain why this condition produces a greater mean value (purple boxes, instantaneous values shown in Figure 36).

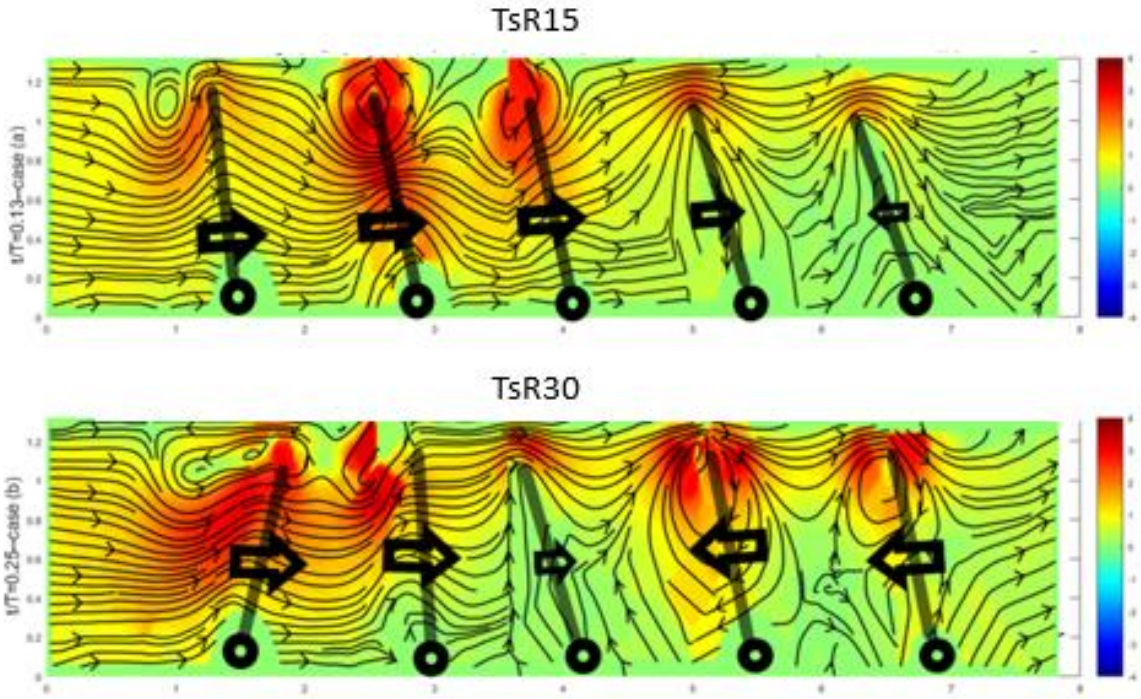

Figure 34.Instantaneous velocity field and streamlines at t/T=0.13 and t/T=0.25 for a) TsR15 b) TsR30

Figure 34 a represents symplectic metachrony with a small phase delay of $\Delta\theta_i = +15°$ (TsR15) for the case (a) , and higher phase delay of $\Delta\theta_i = +30°$ (TsR30) for case b. At *t/T*=0.13, plates 1 through 4 are executing their effective stroke, with the positive net flow to the right. Plate 5 is at the end of recovery stroke and is about to start its effective stroke. *t/T* =0.13 is selected to represent TsR15 because positive pumping performance occurs at this time. Effective pumping starts earlier for TsR15 due to the smaller phase lag between adjacent plates: A greater number of plates start

contributing to positive flow sooner for $\Delta\theta_i$ = +15°condition than the $\Delta\theta_i$ = +30°. Effective pumping won't be starting for TsR30 until *t/T*~0.25, at which time 2 plates are in effective stroke to the right. Even though effective pumping starts earlier for $\Delta\theta_i = +15°$, around t/T~ 0.13, the total effective pumping time period is 17% longer for $\Delta\theta_i = +30°$ because of the gradual decay of pumping curve in Figure 37. In the (b), at *t/T* = 0.25, two plates are in effective stroke and the third plate is stationary at end of recovery stroke. Plates 4 and 5 are in the recovery stroke, hence CW rotational cells are formed at the plates tip location. Clockwise vortices help the pumping by shielding the negative flow from the positive stream as discussed for the antiplectic case discussed earlier. It is seen that all negative flow from plates 4, and 5 are obscured by positive flow from plates 1 and 2.

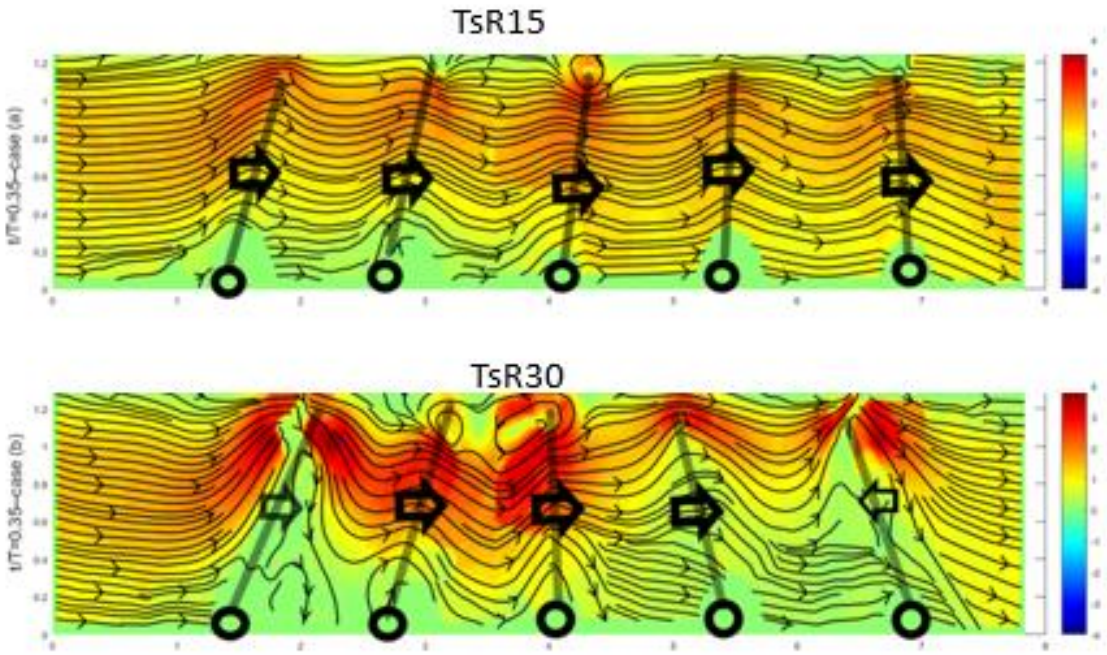

Figure 35.Instantaneous velocity field and streamlines at t/T=0.4 for a) TsR15 b) TsR30

In Figure 35, all the plates are in their effective stroke for TsR15 **,** which results in a steady strong flow in the pumping direction and the highest pumping performance in the Figure 33. In the TsR30, plates 1 through 4 are in effective stroke with the plate 1 is decelerating at the end of stroke. Plate 5 is transitioning from recovery to effective stroke. The pumping performance at this instant is higher for TsR15 in comparison to TsR30.

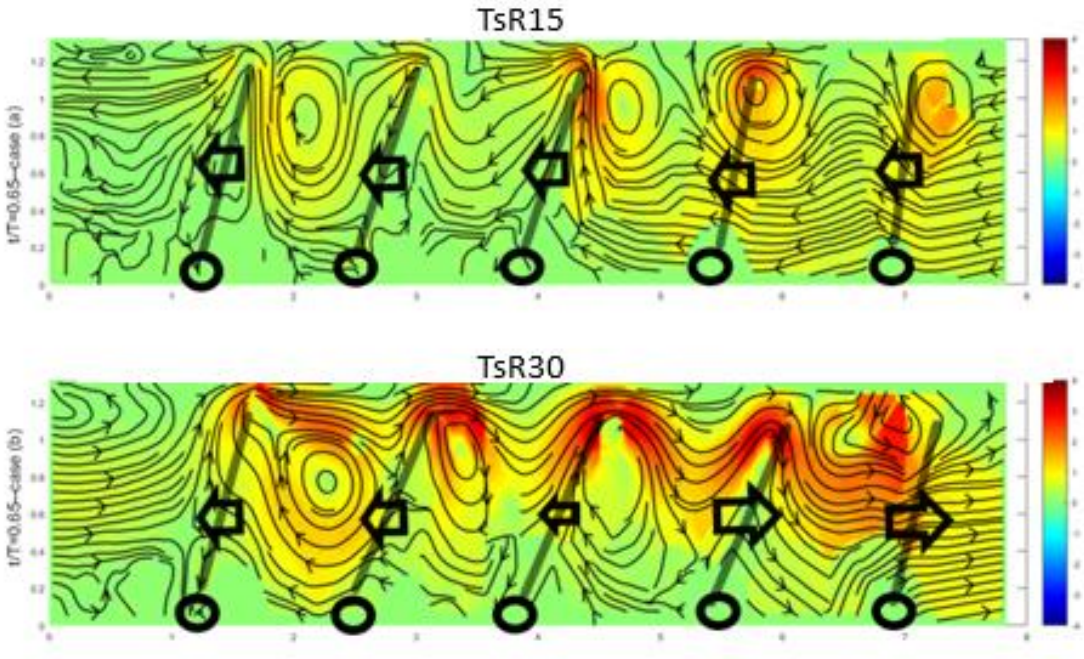

Figure 36.Instantaneous velocity field and streamlines at t/T=0.68 for a) TsR15 b) TsR30

At the t/T=0.68 in the Figure 36, all the plates in TsR15 are in recovery stroke contribute to the negative flow. In TsR30, however, plates 4 and 5 are in their effective stroke. This phase demonstrates the reason behind the prolonged effective pumping period in TsR30 which contributes to the higher pumping performance.

namely, plates 1, 2, and 3 are in the recovery stroke and clockwise vortices are formed which again help the positive flow by shielding the negative flow. Plates 4 and 5 are in the effective stroke which provides positive pumping performance unlike TsR15 at this phase. To finish out the observations of the flow field, the time-averaged velocity magnitude and streamlines of different asymmetrical triangle cases are shown in Figure 37.

Figure 37 a) represents TR0, b)TsR15, c)TsR30, d)TAR15, and e) is TAR30.

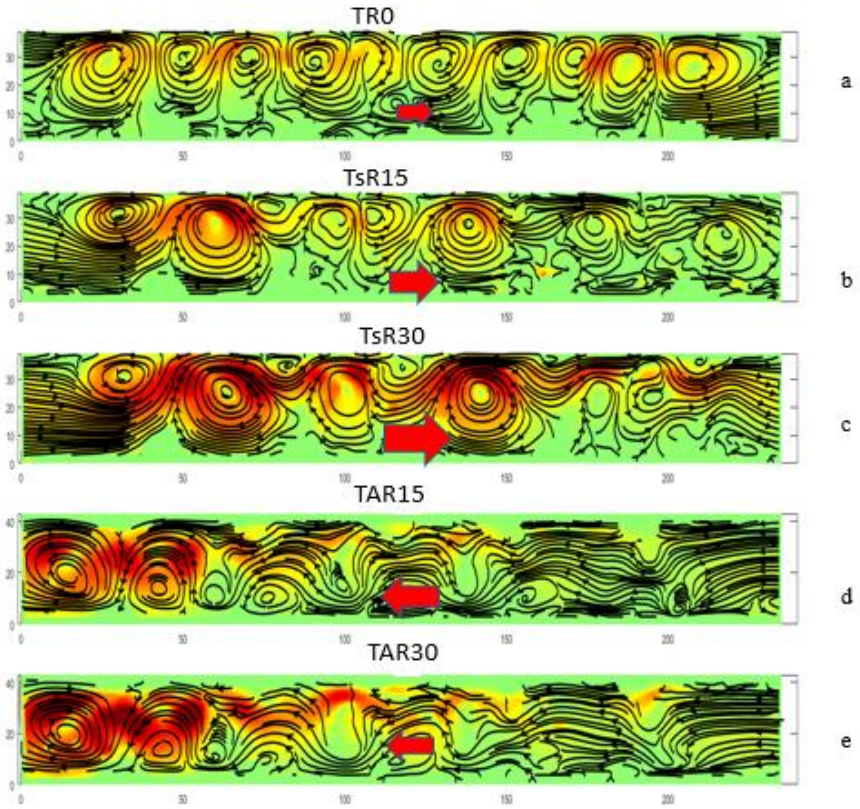

Figure 37. time-averaged fields of the different asymmetrical triangle cases a) TR0, b)TsR15, c)TsR30, d)TAR15, e) TAR30. The Red arrows demonstrate the pumping direction.

The synchronous case TR0 in Figure 37a, is noted to consists of compact counter-rotating/inter connected vortices with weak pumping direction to the right. TsR15 and TsR30 (Figure 37 b,c) demonstrate travelling metachronal wave from left to right in the direction of pumping (red arrow). Metachronal wave in TsR30 travels longer distance in comparison to TsR15.

Two antiplectic cases TAR15 and TAR30 (Figure 37 d,e) exhibit reversed pumping direction in which pumping performance of TAR15 is slightly higher than TAR30.

Dissipation and work and energy equations

Dissipation rate

In the previous section pumping performance is introduced as a means to quantify the relative output of a simple 5 plate pump, and found that for the fixed intermediate Reynolds number used in this study, the highest pumping performance was produced using a hinged plate with an antiplectic metachronal motion $\Delta\theta_i = 90$ as an input actuation.

Table 7.Total work at different experimental conditions in an array of 5 oscillating plates

$\Delta\theta_i$ and plate type	Wave form	Metachronal form	Total work	Pumping Performance	MSVF (whole array)	MSVF (per single plate)
0 (rigid)	T0.6 (0.4 Hz)	NA	0.31	0.03	0.01	0.02
15 (rigid)	T0.6 (0.4 HZ)	Antiplectic	0.33	0.05	0.15	0.03
30 (rigid)	T0.6 (0.4 HZ)	Antiplectic	0.4	0.03	0.075	0.015
15 (rigid)	T0.6 (0.4 HZ)	Symplectic	0.23	0.07	0.3	0.06
30 (rigid)	T0.6 (0.4 HZ)	Symplectic	0.41	0.12	0.3	0.06
0 (flexible)	Sine (f=0.6HZ)	NA	0.05	0.05	1	0.2
90 (flexible)	Sine (f=0.6HZ)	Antiplectic	0.12	0.13	0.81	0.16
One gill flexible	f=0.6HZ	NA	0.015	0.03	2	2
One gill rigid	T0.6 (0.4 HZ)	NA	0.0056	0.0097	1.73	1.73

MSVF is calculated and presented for all the multiple plate array tests in Table 7. This measure is our adaptation to present the pumping efficiency and is used to explore the following 3 questions concerning the pumping behavior.

1. Is pumping performance in the array of 5 plates 5x higher than single plate? How about total work?
2. How does flexibility play a role in terms of pumping performance and MSVF?
3. How does the interaction afforded by metachronal motion would influence MSVF?

In general, it is found with the current work that a single plate will have higher MSVF at similar conditions in comparison to the comparable 5 plate array because their total input work is much less than the array. For example, the asymmetric actuation of 5 rigid plates indicates 20x to 40x increases in the required work in comparison to the

single rigid plate. This is compensated somewhat by an increase in the pumping performance, but the pumping does not increase as dramatically, resulting in 6x higher MSVF for a single plate in comparison to symplectic case with $\Delta\theta_i$ =30. Five flexible plates demonstrate relatively higher total work on the order of 3x in synchronous case and 8x in the metachronal motion. $\Delta\theta_i$ =90 will result in higher pumping performance, but higher total work will reduce MSVF in comparison to synchronic case.

Also, in the rigid cases, total work is higher for increased phase lag between adjacent plates for both antiplectic and symplectic motions comparing dissipation rate for $\Delta\theta_i = 15$ and $\Delta\theta_i = 30$. As phase lag between adjacent plates is increased, there will be more inter-plate conflict and more dissipation (total work). Flexible plates with sinusoidal input actuation exhibit the highest pumping performance, which demonstrates the advantage of flexibility both in minimizing the increase in the dissipation rate and increasing the overall pumping performance in an array. Utilizing 5 hinged plates will generate nearly 5 times more pumping in comparison to the single flexible plate**.** $\Delta\theta_i = 30$ in symplectic metachronal motion exhibits the highest pumping performance among triangle input wave cases, which is more than 10 times that provided by a single plate. MSVF of symplectic cases are higher than antiplectic cases mainly due to higher pumping performance for these cases.

To examine some possible specific reasons for the dramatic increase in dissipation, the spatial domain of the array was divided into five different cells, see Figure 38. Each cell consists of one plate a proportional share of the inter-plate volume. The dissipation in this region is compared to the dissipation produced by a comparable single flexible plate.

In Figure 38, plate 3 clearly demonstrates higher dissipation, with plates 2 and 4 approximately 20% less but with a similar spatial distribution. Plates 1 and 5 demonstrate the lowest dissipation. This seems to indicate a clear difference due to the spatial position. Latter will be discussed more in detail in the Figure 40, and Figure 41.

This will answer the following questions: 1. How much Energy input will differ from a single flexible plate experiment to one flexible plate in the array of five plates? 2. What do discrepancies between each cell's dissipation rate tells us? And finally, which part of channel will have higher energy dissipation rate?

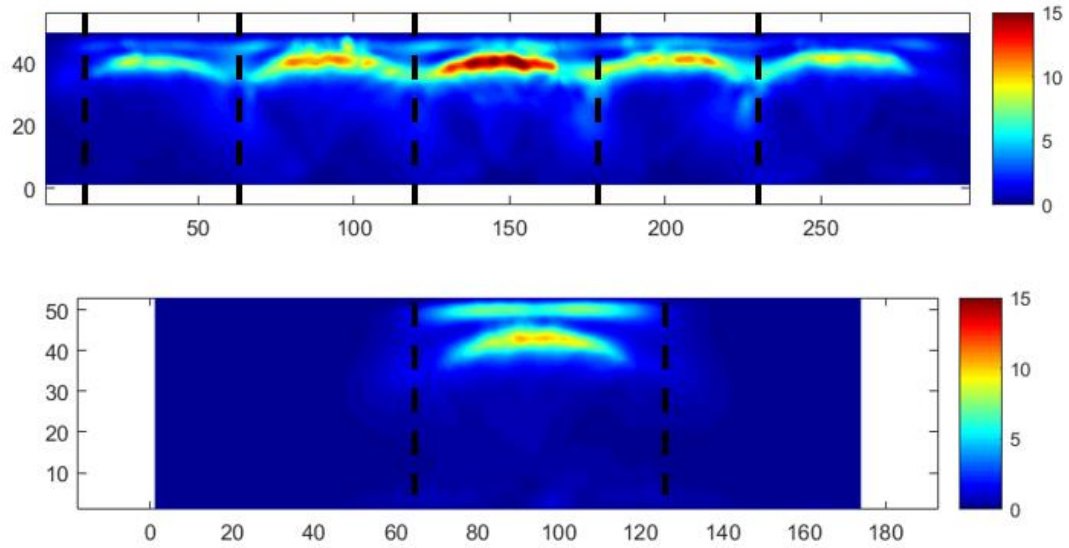

Figure 38.Comparison between one plate in a) SAF90 and b) one flexible plate.

Channel is divided to 5 different cells and all the cells (2 through 5) are compared to first cell and the one flexible plate experiment. We can measure dissipation rate for each cell at each time and study the effect of presence of multiple plates as well as the metachronal input motion in an array.

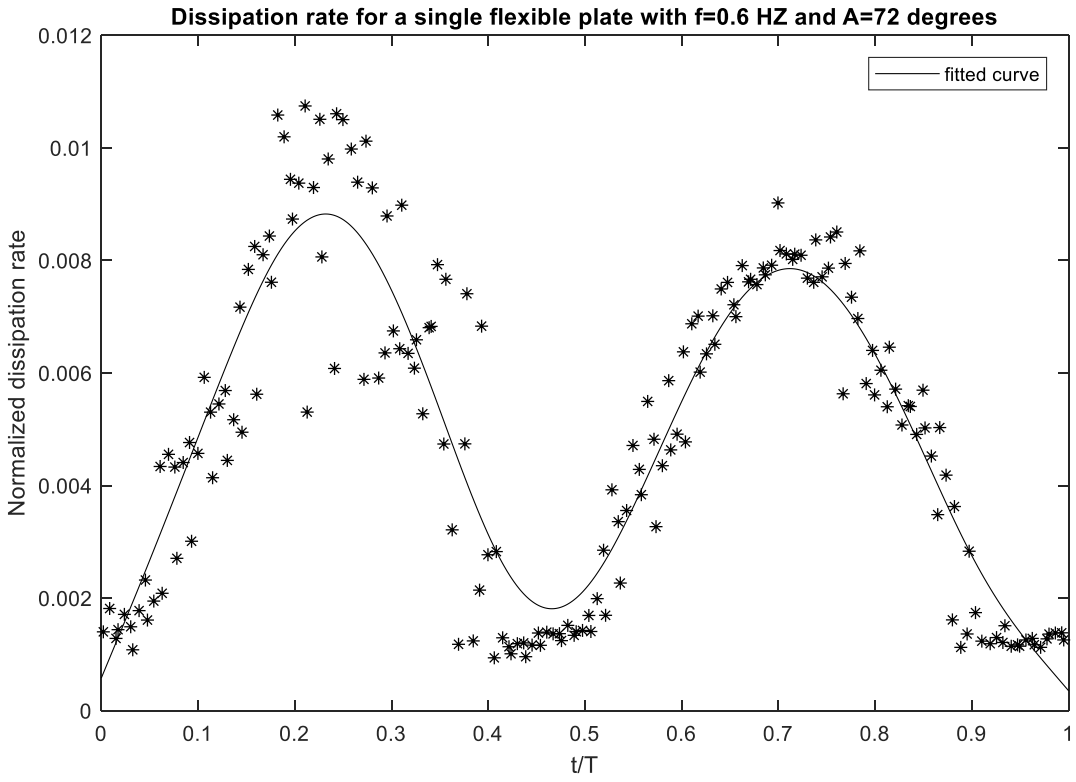

Figure 39.Dissipation rate for a single flexible plate with amplitude of 72 degrees and f=0.6 HZ.

Figure 39 demonstrate dissipation rate for an isolated flexible plate, which has two peaks. The first peak is slightly higher due to the straight plate in the effective stroke and smaller gap between plate's tip and the wall. This will cause more shearing in the flow and increased dissipation rate. The flexible plate bends in the recovery stroke which corresponds to slightly lowered peak. Figure 40 is the comparison of dissipation rate of corresponding to plates 2 through 5 with the reference value obtained from the first plate. Dissipation rate for the first cell is marked in black and other cells are in red. There is a 90 degrees phase lag between the plates in each cell, but for comparison purposes, they have been aligned to synchronize their motions to common parts of the cycle (t/T = 0 corresponds to the beginning of the effective

stroke). Shifting the other plates motion in time permits a more accurate and direct comparison between dissipation rate of different cells. In general, one would expect a relatively close match between the dissipation rates of different cases at similar points of the cycle. This is tempered by the fact that the overall flowrate created by the array is also varying with time, changing the relative motion surrounding each plate at their given phase.

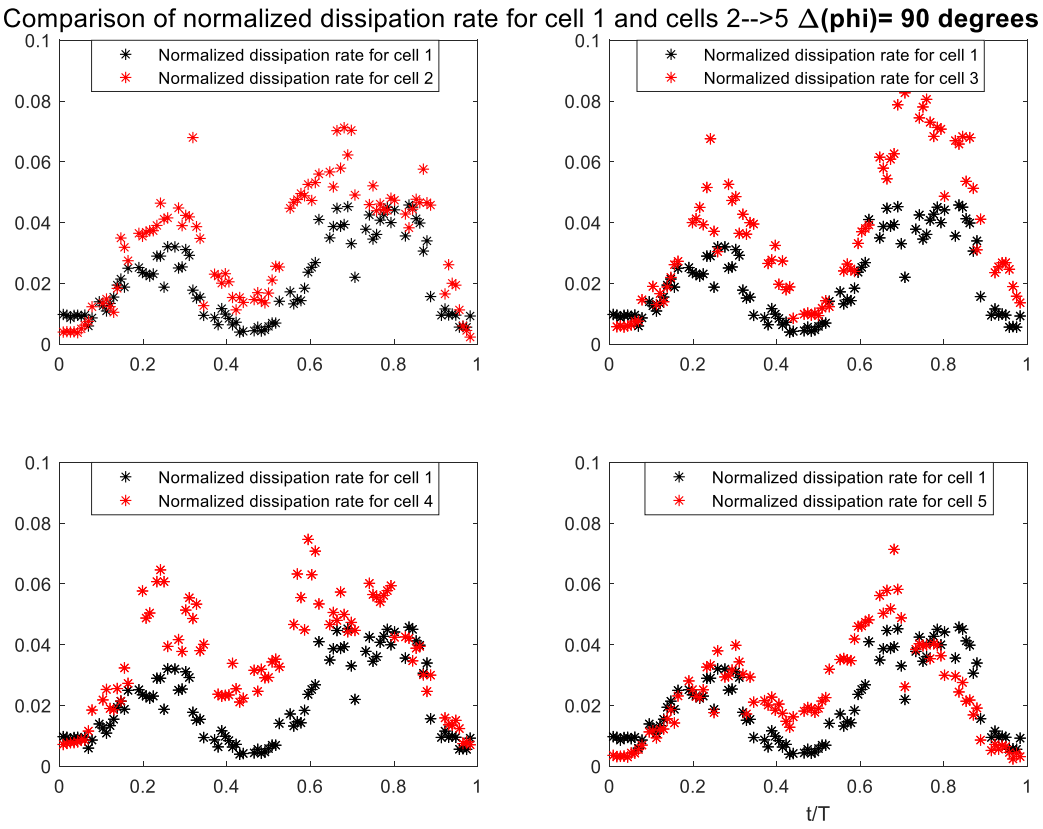

Figure 40.Comparison between dissipation rate in different cells (2.5) and cell 1 in an array of five flexible plates with 90 degrees phase lag between them. A) comparison of cell 1 and cell 2. B) comparison of cell 3 and 4. C) comparison of cell 1 and cell 5.

First of all, unlike the dissipation rate in single flexible plate in the Figure 39 the first peak all of the plates is smaller than the second peak. Secondly, the second peak for the third plate is noticeably higher than other cases by approximately 30% to 50%.

Finally, during the end of the effective stroke and beginning of the recovery stroke for plates 2 though 5, the cell dissipation rate is noticeably higher than the first cell. To help explain these differences, the instantaneous spatial dissipation rate for four different phases in the cycle are shown in Figure 41.

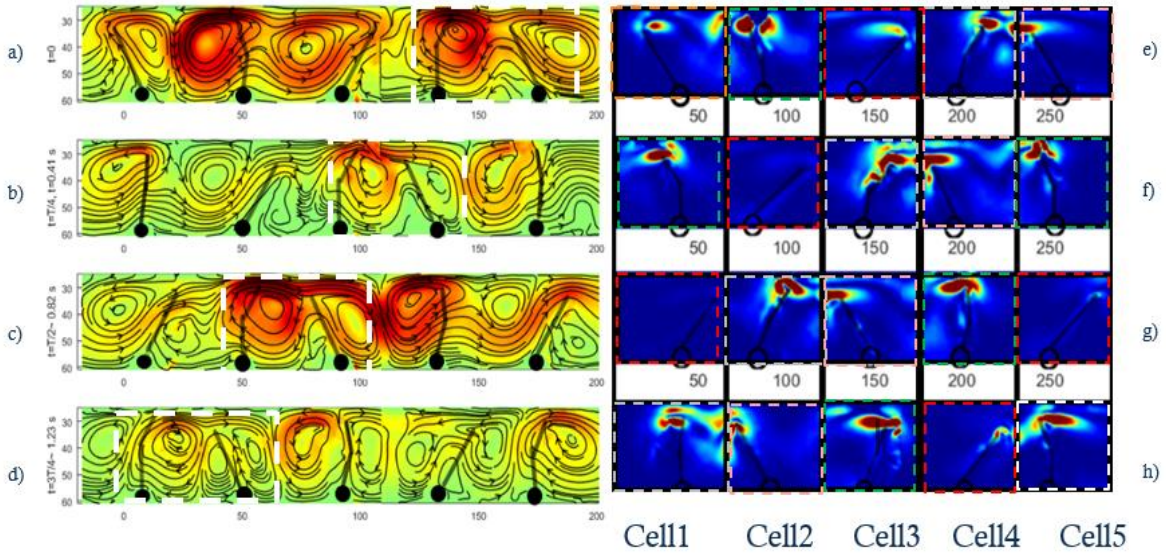

Figure 41. Ensemble-averaged normalized velocity magnitude fields for SAF90 a) ensemble-averaged velocity field at t=0. b) ensemble-averaged velocity field at t=T/4. c) ensemble-averaged velocity field at t=T/2. d) ensemble-averaged velocity field at t=3 T/4 Instantaneous dissipation rate throughout one cycle with 90 degrees phase lag between each contour at e) t=0 f) t=T/4 g) t=T/2 h) t=3 T/4 . White box demonstrate the emergence of dissipation rate from two adjacent plates. Orange, green, red, grey, and pink boxes tracks the dissipation rate for a cells experiencing a similar conditions.

The differences between dissipation rate of different cells in Figure 40 can be explained by looking at instantaneous dissipation contours in Figure 41. In the Figure 41, five different cells are boxed throughout the cycle corresponds to different trends in Figure 40.

The cell averaging regions (grey boxes in Figure 41 e, f, g, and h) from two adjacent flexible plates are merged. Each plate is in the recovery is bent, and the region of higher dissipation rate is merged with the dissipation rate of adjacent plate at the end

of effective stroke. Grey boxes correspond to maximum values in the Figure 40 (second peak values).

Readers may can ask the following question: why does the highest peak occur when plate three bends and passes through middle of the recovery stroke in the figure 41f ? The question can be answered by looking at the velocity contours in Figure 41b, t=T/4. In the case of the highest dissipation value the third plate bends, and it is in the recovery stroke (Figure 41b). The positive flow from plates 1 and 2 from left is carried out to the counter-oscillating plate 3 and therefore it decelerates the flow and cause a high energy dissipation. The negative flow from plate 4 (which finishes recovery stroke) also contributes to higher dissipation rate at T=t/4.

Dissipation rate is lower in the first cell, and it is due to the minimal energy dissipation at the beginning of channel where the interactions between plates are minimal.

Chapter 5: Conclusion

Experiments were conducted with the goal of studying the effect of three different types of asymmetric actuations on the pumping behavior of oscillating plates in a regime at the interface between viscous and inertial dominated flow: 1) temporal asymmetry, 2) spatial asymmetry due to conformal geometry changes of the plate, and 3) spatial asymmetry due to phase shifts in the actuation kinematics within an array of plates. The first condition was implemented utilizing the temporal asymmetry provided by a triangle wave. Secondly, the plate with one-way elastic hinge, will generate non-reciprocal conformal geometry change during the oscillatory motion. Finally, both cases are examined in the context of a multi-plate array. The pumping performance was calculated to measure the cycle-averaged flow rate in the channel, and the dissipation rate was adopted as measure for the total work. For the temporal asymmetry, an increase in the asymmetry parameter resulted in a monotonic increase in the pumping performance as well as the total work required.

In the case of spatial asymmetry due to conformal geometry, single flexible appendage, ($MSVF = \frac{\Pi}{\bar{E}}$) is the highest for the flexible case with the higher frequencies in the same Reynolds numbers. The higher frequency Input Sine wave (f=0.88 HZ) demonstrates higher pumping performance than the higher amplitude sine wave input ($\Delta\Phi$=96), but a slightly decreased dissipation rate (total work) in the same Reynolds number. Increased pumping performance and lower dissipation rate

will result in overall 10% increase in MSVF for the f=0.88 HZ, ΔΦ=54 in comparison to f=0.5 HZ, and ΔΦ=96.

In the case of temporal asymmetry in a rigid plate (triangle waves), $\varepsilon = 0.8$ demonstrate the highest MSVF and pumping performance. Total work is the highest for the $\varepsilon = 0.8$, but noticeable pumping performance (0.12) will compensate and MSVF is increased. Instantaneous dissipation rate indicates two peak values for a flexible case with f=0.88 HZ and ΔΦ=96 in which first peak is higher than the second. The plate is straight in the effective stroke and dissipates more energy, but it bends in the recovery stroke resulting in less momentum transfer and lowered dissipation rate. Proximity to channel upper wall for a straight plate in effective stroke is the second reason for the increased dissipation rate. In the case of symmetrical input actuation in a single rigid plate, the instantaneous dissipation rate indicates two identical peaks for the effective and recovery strokes. As asymmetry is introduced the second peak decreases and is substantially reduced in the cases of the $\varepsilon = 0.6$ and $\varepsilon = 0.8$.

Increasing the number of plates to five will increase the pumping performance. For flexible cases antiplectic metachronal motion with $\Delta\theta_i = -90$, (spatial asymmetry due to phase shifts) demonstrate the highest pumping performance. In general, single plate experiments will have higher MSVF because their total input work is much less than the array. Asymmetric actuation of 5 rigid plates indicates noticeably higher required work in comparison to the single rigid plate. (20x to 40x more input energy is required) which will result in 6x more MSVF for single plate in comparison to symplectic case with $\Delta\theta_i$ =30. $\Delta\theta_i$ =30 demonstrate

12x more pumping than a single rigid plate, but the work required increases even more (the dissipation for that case increased 80x, causing a net decrease in MSVF by about a factor of 6x).

Five flexible plates demonstrate relatively higher total work than single flexible plate in order of 3 times in synchronic case and 8x in $\Delta\theta_i$ =-90. $\Delta\theta_i$ =-90 will result in higher pumping performance, but noticeably higher total work will reduce MSVF in comparison to synchronic case. Instantaneous dissipation in $\Delta\theta_i$ =-90 demonstrate different behavior than single flexible plate. Second peak in the dissipation curve is higher which is due to pumping from adjacent plate and counter-rotating plates in the various sections of channel.

In the rigid cases, in the array of five, total work is higher for increased phase lag between adjacent plates for both antiplectic and symplectic motions comparing dissipation rate for $\Delta\theta_i = -15$ and $\Delta\theta_i = -30$. As phase lag between adjacent plates is increased there will be more hydrodynamic interaction between counter-rotating plates (deviation from synchronic case) and more dissipation rate (total work).

Pumping performance for $\Delta\theta_i = -30$ is higher for symplectic case in which shielding effect plays a role. Negative flow is the plates in the recovery stroke will generate CW vortices and shield the negative flow from stronger positive stream.

Flexible plates with input sine wave exhibit the highest pumping performance which demonstrate the advantage of flexibility both in reducing the dissipation rate and increasing the pumping performance in an array. Shielding effect is more

pronounce in the case of flexible plates in array of five and will improve the pumping performance.

Five flexible plates with $\Delta\theta_i = -90$ will generate more than 4 times more pumping in comparison to the single flexible plate. $\Delta\theta_i = -30$ in asymmetric triangle actuation and symplectic metachronal motion exhibits the highest pumping performance among different triangle input cases which is more than 10 times of using a single rigid plate.

Current work suggests a feasible methodology to study the complicated intermediate Reynolds number regime. Increased pumping performance can be directly related to the detail of the flow structure and the interaction of shed vortices from appendages. Calculating dissipation rate also provides a beneficial detail that can be used to optimize appendicular pumps in a variety of ranges. For example, with knowledge we obtained from the energy dissipation in the case of five flexible plates in sine actuation and $\Delta\theta_i = -90$, we conclude that More energy is dissipated in the third cell.

Appendices

Appendix A: Justification of dissipation as measure of the work input

Following development by Kundu *et al*. (2002), the mechanical energy equation is first obtained by taking the dot product of $u_i$and momentum equation to obtain:

$$\rho \frac{D}{Dt}\left(\frac{1}{2}u_i^2\right) = \rho u_i g_i + u_i \frac{\partial \tau_{ij}}{\partial x_j} \quad (20)$$

Where u_i is velocity vector and g_i is gravity and τ_{ij} is shear force.

Equation (20) is the simplest form of the mechanical energy equation. Equation (20) therefore says that the rate of increase of kinetic energy at a point is equal to the sum of the rate of work done by body force g and the rate of work done by the net surface force $u_i \frac{\partial \tau_{ij}}{\partial x_j}$ per unit volume.

If we multiply the continuity equation by $\frac{\rho u^2}{2}$, we will get:

$$\frac{1}{2}\rho u_i^2 \left[\frac{\partial \rho}{\partial t} + \frac{\partial}{\partial x_j}(\rho u_j)\right] = 0 \quad (21)$$

If we add the equation (21) to (20) and substitute $\frac{\rho {u_i}^2}{2}$ by E, we will get:

$$\frac{\partial E}{\partial t} + \nabla.(uE) = \rho u_i g_i + u_i.\left(\nabla.\tau_{ij}\right) \quad (22)$$

Working out the last term of eq 22 can be done by physically understanding the concept of deformation work and viscous dissipation. Pressure term appears in τ_{ij} by substituting from Newtonian constitutive in eq.22 We can examine $u_i(\frac{\partial \tau_{ij}}{\partial x_j})$ to determine how kinetic energy can be transformed (lost) to the internal energy by

deformation of fluid elements. In equation (20) the term $u_i(\frac{\partial \tau_{ij}}{\partial x_j})$ is velocity times the net force imbalance at a point due to differences of stress on opposite faces of an element; The net force will accelerate the fluid hence increase its kinetic energy. But it does not take to the account the work due to pure deformation of fluid element. The total work rate per volume at a point can be split up into two components:

$$\underbrace{\frac{\partial}{\partial x_j}(u_i \tau_{ij})}_{\text{Total work (rate/volume)}} = \underbrace{\tau_{ij}\frac{\partial u_i}{\partial x_j}}_{\text{Deformation work (rate/volume)}} + \underbrace{u_i \frac{\partial \tau_{ij}}{\partial x_j}}_{\text{Increase of KE}} \quad (23)$$

$u_i \frac{\partial \tau_{ij}}{\partial x_j}$ will only accelerate the element without accounting for the deformation work.

The remaining term in equation (23), $\tau_{ij}\frac{\partial u_i}{\partial x_j}$, will present deformation work.

The deformation work rate can be rewritten using the symmetry of the stress tensor. The product $\tau_{ij}\frac{\partial ui}{\partial xj}$ is therefore equal to τ_{ij} multiplied by the symmetric part of $(\frac{\partial ui}{\partial xj})$ which is e_{ij}.

$$Deformation\ work\ per\ volume = \tau_{ij}\frac{\partial u_i}{\partial x_j} = \tau_{ij}\, e_{ij} \quad (24)$$

Substitution of Newtonian constitutive equation gives:

$$\tau_{ij} = -p\delta_{ij} + 2\mu e_{ij} - \frac{2}{3}\mu(\nabla . u_i)\delta_{ij} \quad (25)$$

Substituting 25 in 24 will result in:

Deformation work= $-p(\nabla.u_i) + 2\mu\, e_{ij}e_{ij} - \frac{2}{3}\mu(\nabla.u_i)^2$ (26)

Deformation work (rate per volume)= $-p(\nabla.u_i) + \phi$ (27)

Where

$$\phi = 2\mu e_{ij}\, e_{ij} - \frac{2}{3}\mu(\nabla.u_i)^2 = 2\mu\left[e_{ij} - \frac{1}{3}\,(\nabla.u_i)\delta_{ij}\right]^2 \quad (28)$$

In order to rewrite eq. (20) in terms of ϕ, we first rewrite eq. (20) in terms of:

$$\frac{1}{2}\rho\frac{D{u_i}^2}{Dt} = \rho u_i.g_i + \frac{\partial}{\partial x_j}\left(u_i.\tau_{ij}\right) - \tau_{ij}e_{ij} \quad (29)$$

Where we used ($\tau_{ij}(\frac{\partial ui}{\partial xj})$=$\tau_{ij}\, e_{ij}$). using eq.20 to rewrite the deformation work rate per volume Eq.29 becomes:

$$\rho\frac{D}{Dt}\left(\frac{1}{2}u_i^2\right) = \underbrace{\rho u_i.g_i}_{\text{Rate of work by body work}} \quad \underbrace{\frac{\partial}{\partial x_j}\left(u_i\tau_{ij)}\right)}_{\text{Rate of work by } \tau} + \underbrace{p(\nabla.u_i)}_{\text{Rate of work by volume expansion}} - \underbrace{\phi}_{\text{Rate of viscous dissipation}} \quad (30)$$

The viscous dissipation term is always positive and represents a rate of loss of mechanical energy and a gain of internal energy due to deformation of the element. The term $\tau_{ij}e_{ij} = p * (\nabla.\mathrm{u}) - \emptyset$ represents the total deformation work rate per volume.

We can integrate the latter relationship (30) in a fixed volume for an array of oscillating plates in the channel

Figure 42 depicts the schematic of oscillating plate in a channel and the blue line represents the control volume of interest.

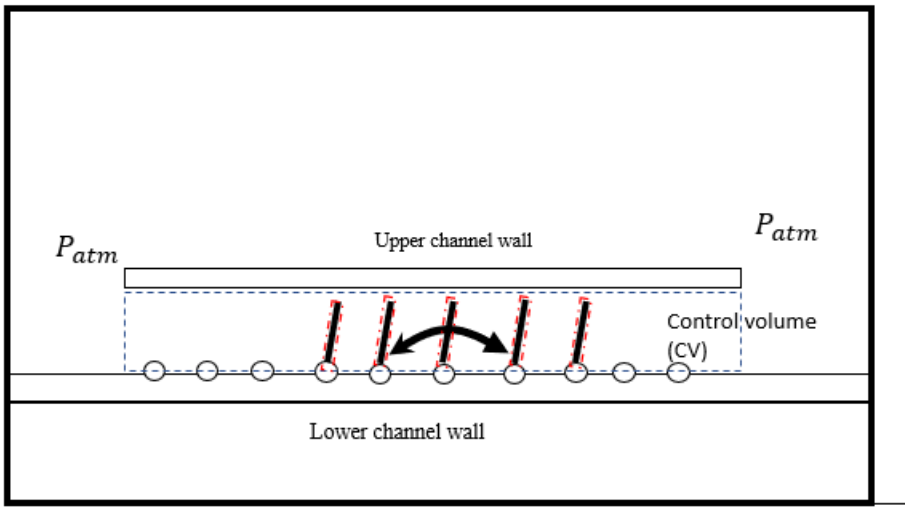

Figure 42.Oscillating plate in the channel and corresponding control volume.

We can apply the integral form of Eq (30) to our control volume and solve for a surface shear force term on our plates.

$$\frac{d}{dt}\int\left(\frac{\rho}{2}u_i u_i\right)dV + \int\left(\frac{\rho}{2}u_i u_i\right)u_j n_j dA = \int_{CS} u_i \tau_{ij} n_j dA + \int_{plates} u_i \tau_{ij} n_j dA - \int \phi \quad (31)$$

1	2	3	4	5

1. Rate of change of Kinetic Energy in the control volume: This term will be high when unsteadiness is sinificant in high Reynolds numbers.
2. Rate of outflow across boundary: This energy outflow across the boundary. And it will be shown that it is negligible.
3. Rate of work by surface force at the control surface boundaries: This term includes pressure term which we cannot calculate from our PIV data but we can approximate by Poiseuille flow which will negligibly small for our problem. The channel is place in the bigger tank which is open to the environment with the atmospheric pressure. This suggests a minor pressure gradient.
4. Rate of work by surface force at plates: we need to calculate this term which is according to figure 43 is predominantly equal to dissipation rate.

Rate of viscous dissipation

Calculating all the terms in the Eq (32) and a plot of over one cycle is shown in the Figure 43 for the case of TRs15.

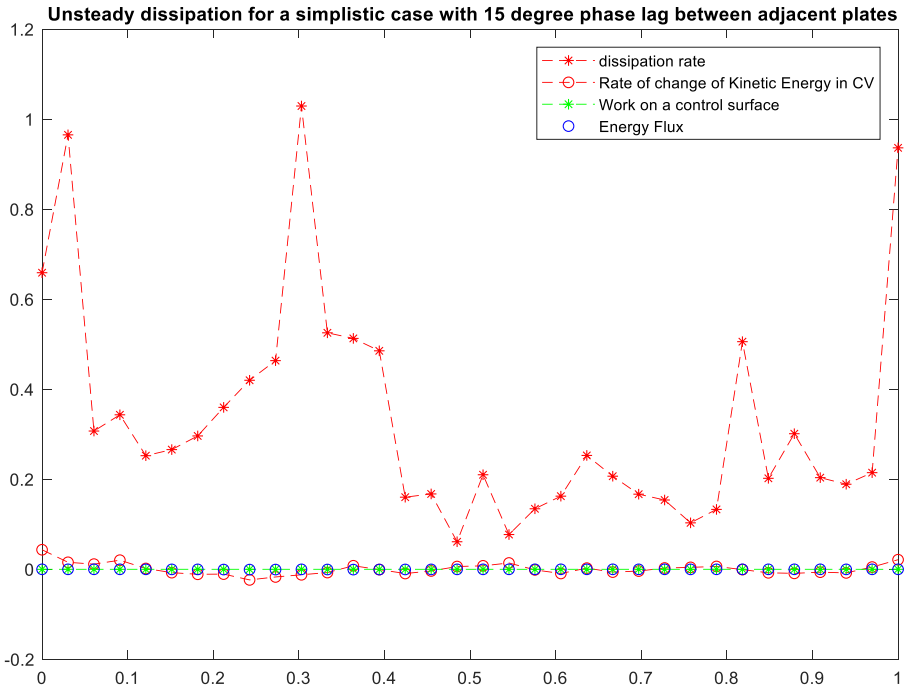

Figure 43) Different energy rate terms in the control volume for Symplectic metachronal motion in an array of five rigid plates.

Figure 43 is constructed by calculating all the terms in Eq 31 from PIV data. As it is seen terms 1,2, and 3 are negligibly small in comparison to dissipation rate and our assumption of using (∅) as a replacement for a total work is valid.

Appendix A: Selection of 2D cases for the thesis

Table 8 to table 13 demonstrate different experiments in oil and glycerin. We check two-dimensionality for all the cases and accept those in which 3D effects were less than 10%. These cases are marked in yellow in which discrepancies between pumping inflow and outflow were less than 10% for the cases marked in yellow. Cases in yellow were presented in this thesis. Tables 12 and 13 visually did not satisfy conservation of mass.

Table 8. 3D effects in an array of five rigid plates in the presence of sine wave

cases	3D effects	
R1100	5%	5 Rigid plates, F=0.6 HZ, A=72 degrees, $\Delta\varphi = 0$
R1190	13%	5 Rigid plates, F=0.6 HZ, A=72 degrees, $\Delta\varphi = 90$
RS1100	8%	5 Rigid plates, $\varepsilon \sim 0.8$, $\Delta\varphi = 0$
R11270	15%	5 Rigid plates, F=0.6 HZ, A=72 degrees, $\Delta\varphi = 270$
R11180	21%	5 Rigid plates, F=0.6 HZ, A=72 degrees, $\Delta\varphi = 180$
RS1190	43%	5 Rigid plates, $\varepsilon \sim 0.8$, A=72 degrees, $\Delta\varphi = 90$
RS11180	67%	5 Rigid plates, $\varepsilon \sim 0.8$, A=72 degrees, $\Delta\varphi = 180$

Table 9. 3D effects in an array of five flexible plates in the presence of sine wave

cases	3D effect	
F1100	3%	5 flexible plates, F=0.6 HZ, A=72 degrees, $\Delta\varphi = 0$
F1190	7%	5 flexible plates, F=0.6 HZ, A=72 degrees, $\Delta\varphi = 90$
FS1100	14%	5 flexible plates, $\varepsilon \sim 0.8$, A=72 degrees, $\Delta\varphi = 0$
F11270	17%	5 flexible plates, F=0.6 HZ, A=72 degrees, $\Delta\varphi = 270$
F11180	28%	5 flexible plates, F=0.6 HZ, A=72 degrees, $\Delta\varphi = 180$
FS1190	37%	5 flexible plates, $\varepsilon \sim 0.8$, A=72 degrees, $\Delta\varphi = 90$
FS11180	73%	5 flexible plates, $\varepsilon \sim 0.8$, A=72 degrees, $\Delta\varphi = 180$

Table 10. 3D effects in array of five rigid plates in the presence of symplectic triangle wave input

cases	3D effects	
Symp00	5%	5 Rigid plates, Symplectic, $\varepsilon\sim0.6$, A=72 degrees, $\Delta\varphi = 0$
Symp(15)	4%	5 Rigid plates, Symplectic, $\varepsilon\sim0.6$, A=72 degrees, $\Delta\varphi = 15$
Symp(30)	8%	5 Rigid plates, Symplectic, $\varepsilon\sim0.6$, A=72 degrees, $\Delta\varphi = 30$
Symp(60)	13%	5 Rigid plates, Symplectic, $\varepsilon\sim0.6$, A=72 degrees, $\Delta\varphi = 60$
Symp(90)	25%	5 Rigid plates, Symplectic, $\varepsilon\sim0.6$, A=72 degrees, $\Delta\varphi = 90$

Table 11. 3D effects in an array of five rigid plates in the presence of antiplectic triangle waave input

cases	3D effects	
Ant(15)	6%	5 Rigid plates, Antyplectic, $\varepsilon\sim0.6$, A=72 degrees, $\Delta\varphi = 15$
Ant(30)	7%	5 Rigid plates, Antyplectic, $\varepsilon\sim0.6$, A=72 degrees, $\Delta\varphi = 30$
Ant(60)	21%	5 Rigid plates, Antyplectic, $\varepsilon\sim0.6$, A=72 degrees, $\Delta\varphi = 60$
Any(90)	32%	5 Rigid plates, Antyplectic, $\varepsilon\sim0.6$, A=72 degrees, $\Delta\varphi = 90$

Table 12. Experiments in glycirin

cases	3D effect	
F1100	visual	5 flexible plates, F=0.6 HZ, A=72 degrees, $\Delta\varphi = 0$, Glycerin
F1190	visual	5 flexible plates, F=0.6 HZ, A=72 degrees, $\Delta\varphi = 90$, Glycerin
FS1100	visual	5 flexible plates, $\varepsilon\sim0.8$, A=72 degrees, $\Delta\varphi = 0$, Glycerin
F11270	visual	5 flexible plates, F=0.6 HZ, A=72 degrees, $\Delta\varphi = 270$, Glycerin
F11180	visual	5 flexible plates, F=0.6 HZ, A=72 degrees, $\Delta\varphi = 180$, Glycerin
FS1190	visual	5 flexible plates, $\varepsilon\sim0.8$, A=72 degrees, $\Delta\varphi = 90$, Glycerin
FS11180	visual	5 flexible plates, $\varepsilon\sim0.8$, A=72 degrees, $\Delta\varphi = 180$, Glycerin

Table 13. Experiments in the glycirin

cases	3D effect	
F1100	visual	3 flexible plates, F=0.6 HZ, A=72 degrees, $\Delta\varphi = 0$, Glycerin
F1190	visual	3 flexible plates, F=0.6 HZ, A=72 degrees, $\Delta\varphi = 90$, Glycerin
FS1100	visual	3 flexible plates, $\varepsilon \sim 0.8$, A=72 degrees, $\Delta\varphi = 0$, Glycerin
F11270	visual	3 flexible plates, F=0.6 HZ, A=72 degrees, $\Delta\varphi = 270$, Glycerin
F11180	visual	3 flexible plates, F=0.6 HZ, A=72 degrees, $\Delta\varphi = 180$, Glycerin
FS1190	visual	3 flexible plates, $\varepsilon \sim 0.8$, A=72 degrees, $\Delta\varphi = 90$, Glycerin
FS11180	visual	3 flexible plates, $\varepsilon \sim 0.8$, A=72 degrees, $\Delta\varphi = 180$, Glycerin

References

Bäumer, C, R Pirow, and R J Paul. 2000. “Respiratory Adaptations to Running-Water Microhabitats in Mayfly Larvae Epeorus Sylvicola and Ecdyonurus Torrentis, Ephemeroptera.” *Physiological and Biochemical Zoology : PBZ* 73 (1): 77–85. https://doi.org/10.1086/316720.

Beebe, David J., Glennys A. Mensing, and Glenn M. Walker. 2002. “Physics and Applications of Microfluidics in Biology.” *Annual Review of Biomedical Engineering* 4 (1): 261–86. https://doi.org/10.1146/annurev.bioeng.4.112601.125916.

Brennen, C, and H Winet. 1977. “Fluid Mechanics of Propulsion by Cilia and Flagella.” *Annual Review of Fluid Mechanics* 9 (1): 339–98. https://doi.org/10.1146/annurev.fl.09.010177.002011.

Burns, Mark A., Brian N. Johnson, Sundaresh N. Brahmasandra, Kalyan Handique, James R. Webster, Madhavi Krishnan, Timothy S. Sammarco, et al. 1998. “An Integrated Nanoliter DNA Analysis Device.” *Science*. https://doi.org/10.1126/science.282.5388.484.

Childress, James F., Ruth R. Faden, Ruth D. Gaare, Lawrence O. Gostin, Jeffrey Kahn, Richard J. Bonnie, Nancy E. Kass, Anna C. Mastroianni, Jonathan D. Moreno, and Phillip Nieburg. 2002. “Public Health Ethics: Mapping the Terrain.” *The Journal of Law, Medicine & Ethics* 30 (2): 170–78. https://doi.org/10.1111/j.1748-720X.2002.tb00384.x.

Childress, Stephen. 1981. *Mechanics of Swimming and Flying*. Cambridge University Press.

Dabiri, J. O., S. P. Colin, K. Katija, and J. H. Costello. 2010. “A Wake-Based Correlate of Swimming Performance and Foraging Behavior in Seven Co-Occurring Jellyfish Species.” *Journal of Experimental Biology* 213 (8): 1217–25. https://doi.org/10.1242/jeb.034660.

Dudley, Robert. 2002. *The Biomechanics of Insect Flight: Form, Function, Evolution*. *Princeton University Press*.

Eriksen, C. H. 1968. “Ecological Significance of Respiration and Substrate for Burrowing Ephemeroptera.” *Canadian Journal of Zoology* 46 (1): 93–103. https://doi.org/10.1139/z68-015.

Eriksen, C. H., and J. E. Mœur. 1990. “Respiratory Functions of Motile Tracheal Gills in Ephemeroptera Nymphs, As Exemplified by Siphlonurus Occidentals Eaton.” *Mayflies and Stoneflies: Life Histories and Biology.Series Entomologica* 44: 109–18.

Gauger, Erik, and Holger Stark. 2006. “Numerical Study of a Microscopic Artificial Swimmer.” *Physical Review E - Statistical, Nonlinear, and Soft Matter Physics* 74 (2). https://doi.org/10.1103/PhysRevE.74.021907.

Gray, J., and G. J. Hancock. 1955. “The Propulsion of Sea-Urchin Spermatozoa.” *Journal of Experimental Biology* 32 (4): 802–14. http://jeb.biologists.org/content/32/4/802%5Cnhttp://jeb.biologists.org/content/32/4/802.full.pdf.

Khaderi, S. N., J. M.J. Den Toonder, and P. R. Onck. 2011. “Microfluidic Propulsion by the Metachronal Beating of Magnetic Artificial Cilia: A Numerical

Analysis." *Journal of Fluid Mechanics* 688: 44–65. https://doi.org/10.1017/jfm.2011.355.
Khaderi, S. N., J. M J den Toonder, and P. R. Onck. 2012. "Fluid Flow due to Collective Non-Reciprocal Motion of Symmetrically-Beating Artificial Cilia." *Biomicrofluidics* 6 (1). https://doi.org/10.1063/1.3676068.
Lamb, Sir Horace. 1932. *Hydrodynamics*. *Cambridge University Press*.
Larson, Andrew J., Kyle C. Stover, and Christopher R. Keyes. 2012. "Effects of Restoration Thinning on Spatial Heterogeneity in Mixed-Conifer Forest." *Canadian Journal of Forest Research* 42 (8): 1505–17. https://doi.org/10.1139/x2012-100.
Larson, Mary, Ken T. Kiger, Khaled Abdelaziz, and Elias Balaras. 2014. "Effect of Metachronal Phasing on the Pumping Efficiency of Oscillating Plate Arrays." *Experiments in Fluids* 55 (5). https://doi.org/10.1007/s00348-014-1741-5.
Laser, D. J., and J. G. Santiago. 2004. "A Review of Micropumps." *Journal of Micromechanics and Microengineering*. https://doi.org/10.1088/0960-1317/14/6/R01.
Lighthill, James. 1976. "Flagellar Hydrodynamics." *SIAM Review* 18 (2): 161–230. https://doi.org/10.1137/1018040.
Lighthill, Sir James. 1975. *Mathematical Biofluiddynamics*. Philadelphia: Society for industrial and applied mathematics (SIAM). http://www.siam.org/journals/ojsa.php.
Lilienthal, a., a. Zell, M. Wandel, and U. Weimar. 2001. "Sensing Odour Sources in Indoor Environments without a Constant Airflow by a Mobile Robot." *Proceedings 2001 ICRA. IEEE International Conference on Robotics and Automation (Cat. No.01CH37164)* 4: 1–6. https://doi.org/10.1109/ROBOT.2001.933243.
Manuel, J. L., and M. J. Dadswell. 1993. "Swimming of Juvenile Sea Scallops, Placopecten Magellanicus (Gmelin): A Minimum Size for Effective Swimming?" *Journal of Experimental Marine Biology and Ecology* 174 (2): 137–75. https://doi.org/10.1016/0022-0981(93)90015-G.
Motani, Ryosuke. 2002. "Scaling Effects in Caudal Fin Propulsion and the Speed of Ichthyosaurs." *Nature* 415 (6869): 309–12. https://doi.org/10.1038/415309a.
Nawroth, Janna C., and John O. Dabiri. 2014. "Induced Drift by a Self-Propelled Swimmer at Intermediate Reynolds Numbers." *Physics of Fluids* 26 (9). https://doi.org/10.1063/1.4893537.
Purcell, Em. 1977. "Life at Low Reynolds Number." *American Journal of Physics*. https://doi.org/10.1119/1.10903.
Sapsford, Ruth. 2001. "The Pelvic Floor: A Clinical Model for Function and Rehabilitation." *Physiotherapy*. https://doi.org/http://dx.doi.org/10.1016/S0031-9406(05)61107-8.
Schilling, Eric A., Andrew Evan Kamholz, and Paul Yager. 2002. "Cell Lysis and Protein Extraction in a Microfluidic Device with Detection by a Fluorogenic Enzyme Assay." *Analytical Chemistry* 74 (8): 1798–1804. https://doi.org/10.1021/ac015640e.
Sensenig, A, Kenneth T. Kiger, and Jeffrey Shultz. 2010. "Transitional Ventilation Mechanisms in Nymphal Mayfly Centroptilum Triangulifer." *Journal of*

Experimental Biology 213 (19): 3319–31.
Sensenig, Andrew T., Kenneth T. Kiger, and Jeffrey W. Shultz. 2009. "The Rowing-to-Flapping Transition: Ontogenetic Changes in Gill-Plate Kinematics in the Nymphal Mayfly Centroptilum Triangulifer (Ephemeroptera, Baetidae)." *Biological Journal of the Linnean Society* 98 (3): 540–55. https://doi.org/10.1111/j.1095-8312.2009.01314.x.
Sleigh, Michael A., John R. Blake, and Nadav Liron. 1988. "The Propulsion of Mucus by Cilia." *American Review of Respiratory Disease* 137 (3): 726–41. https://doi.org/10.1164/ajrccm/137.3.726.
Spedding, G. R., M. Rosén, and A. Hedenström. 2003. "A Family of Vortex Wakes Generated by a Thrush Nightingale in Free Flight in a Wind Tunnel over Its Entire Natural Range of Flight Speeds." *Journal of Experimental Biology* 206 (14): 2313–44. https://doi.org/10.1242/jeb.00423.
Strathmann, R R. 1993. "Hypotheses on the Origins of Marine Larvae." *Annual Review of Ecology and Systematics* 24 (1993): 89–117. https://doi.org/10.1146/annurev.es.24.110193.000513.
Tang, Akaysha C., Barak A. Pearlmutter, Natalie A. Malaszenko, and Dan B. Phung. 2002. "Independent Components of Magnetoencephalography: Single-Trial Response Onset Times." *NeuroImage* 17 (4): 1773–89. https://doi.org/10.1006/nimg.2002.1320.
Taylor, Geoffrey. 1951. "Analysis of the Swimming of Microscopic Organisms." *Proceedings of the Royal Society of London. Series A, Mathematocal and Physical Sciences* 209 (1099): 447–61.
Vitko, Stefan, Helio Tedesco, Josette Eris, Julio Pascual, John Whelchel, John C. Magee, Scott Campbell, et al. 2004. "Everolimus with Optimized Cyclosporine Dosing in Renal Transplant Recipients: 6-Month Safety and Efficacy Results of Two Randomized Studies." *American Journal of Transplantation* 4 (4): 626–35. https://doi.org/10.1111/j.1600-6143.2004.00389.x.
Walker, J. A. 2002. "Functional Morphology and Virtual Models: Physical Constraints on the Design of Oscillating Wings, Fins, Legs, and Feet at Intermediate Reynolds Numbers." *Integrative and Comparative Biology* 42 (2): 232–42. https://doi.org/10.1093/icb/42.2.232.
Whitesides, George M. 2006. "The Origins and the Future of Microfluidics." *Nature*. https://doi.org/10.1038/nature05058.
Wingfield, C A. 1939. "The Function of the Gills of Mayfly Nymphs from Different Habitats." *Journal of Experimental Biology* 16 (3): 363–73. http://jeb.biologists.org/content/16/3/363.abstract.